

This is a work of the United States Government. In accordance with 17 U.S.C. 105, no copyright protection is available for such works under U.S. Law.

Public Domain Mark 1.0

<https://creativecommons.org/publicdomain/mark/1.0/>

Access to this work was provided by the University of Maryland, Baltimore County (UMBC) ScholarWorks@UMBC digital repository on the Maryland Shared Open Access (MD-SOAR) platform.

Please provide feedback

Please support the ScholarWorks@UMBC repository by emailing scholarworks-group@umbc.edu and telling us what having access to this work means to you and why it's important to you. Thank you.

RESEARCH ARTICLE

10.1002/2017JD026840

Special Section:

Quantifying the emission, properties, and diverse impacts of wildfire smoke

Key Points:

- A method to mitigate fire emission estimation uncertainty from satellite limitations in sampling fires due to clouds, view angles, and swath gaps
- The method is applied to FEER emission using MODIS-based FRP, and both adjusted and original emissions are applied to WRF-Chem modeling
- Evaluation using MODIS, CALIOP, and AERONET data shows that the adjusted emissions render better WRF-Chem simulations of smoke both spatially and temporally

Correspondence to:

J. Wang and Y. Wang,
jun-wang-1@uiowa.edu;
yi-wang-4@uiowa.edu

Citation:

Wang, J., Yue, Y., Wang, Y., Ichoku, C., Ellison, L., & Zeng, J. (2018). Mitigating satellite-based fire sampling limitations in deriving biomass burning emission rates: Application to WRF-Chem model over the Northern sub-Saharan African Region. *Journal of Geophysical Research: Atmospheres*, 123, 507–528. <https://doi.org/10.1002/2017JD026840>

Received 23 MAR 2017

Accepted 8 DEC 2017

Accepted article online 14 DEC 2017

Published online 11 JAN 2018

Mitigating Satellite-Based Fire Sampling Limitations in Deriving Biomass Burning Emission Rates: Application to WRF-Chem Model Over the Northern sub-Saharan African Region

Jun Wang^{1,2,3} , Yun Yue¹, Yi Wang^{2,3}, Charles Ichoku⁴, Luke Ellison^{4,5}, and Jing Zeng²
¹Department of Earth and Atmospheric Sciences, University of Nebraska–Lincoln, Lincoln, NE, USA, ²Department of Chemical and Biochemical Engineering, University of Iowa, Iowa City, IA, USA, ³Center for Global and Regional Environmental Research, University of Iowa, Iowa City, IA, USA, ⁴Climate and Radiation Laboratory, NASA Goddard Space Flight Center, Greenbelt, MD, USA, ⁵Science Systems and Applications, Inc., Lanham, MD, USA

Abstract Largely used in several independent estimates of fire emissions, fire products based on MODIS sensors aboard the Terra and Aqua polar-orbiting satellites have a number of inherent limitations, including (a) inability to detect fires below clouds, (b) significant decrease of detection sensitivity at the edge of scan where pixel sizes are much larger than at nadir, and (c) gaps between adjacent swaths in tropical regions. To remedy these limitations, an empirical method is developed here and applied to correct fire emission estimates based on MODIS pixel level fire radiative power measurements and emission coefficients from the Fire Energetics and Emissions Research (FEER) biomass burning emission inventory. The analysis was performed for January 2010 over the northern sub-Saharan African region. Simulations from WRF-Chem model using original and adjusted emissions are compared with the aerosol optical depth (AOD) products from MODIS and AERONET as well as aerosol vertical profile from CALIOP data. The comparison confirmed an 30–50% improvement in the model simulation performance (in terms of correlation, bias, and spatial pattern of AOD with respect to observations) by the adjusted emissions that not only increases the original emission amount by a factor of two but also results in the spatially continuous estimates of instantaneous fire emissions at daily time scales. Such improvement cannot be achieved by simply scaling the original emission across the study domain. Even with this improvement, a factor of two underestimations still exists in the modeled AOD, which is within the current global fire emissions uncertainty envelope.

Plain Language Summary Polar-orbiting satellites sensors, such as MODIS, have limitations in detecting fires under clouds or when viewing angles are large or in the gaps among satellites' different ground swaths. Here we developed an empirical method to mitigate the effect of these limitations in fire emission estimate. The method is applied to a fire emission inventory (FEER) based on MODIS. We show that, with our method, the adjusted emission inventory improves WRF-Chem simulation of smoke transport and distribution.

1. Introduction

Emissions from biomass burning are generating growing interest from the scientific community and the general public alike because worldwide biomass burning contributes large amounts of greenhouse gases and other trace gases such as carbon dioxide (CO₂), carbon monoxide (CO), nitric oxide (NO), and methane (CH₄), as well as particulates into the atmosphere (Andreae, 1991; Brass et al., 1996; Crutzen & Andreae, 1990; Hao & Liu, 1994; Heald et al., 2003; Ichoku & Ellison, 2014; Shi, Matsunaga, & Yamaguchi, 2015). Gaseous and particulate emissions from biomass burning not only affect local air quality but are also transported in the atmosphere often over long distances to downwind regions, where they can contribute to the degradation of visibility and air quality (Wang et al., 2006). Increased levels of particulate concentration from biomass burning are believed to cause serious human health and public safety issues (Hyer, Wang, & Arellano, 2012; Lighty, Veranth, & Sarofim, 2000). Furthermore, some of these emissions (particularly CO₂, CH₄, and smoke particles) play a significant role in altering the regional and global climate (Crutzen & Andreae, 1990; Wang et al., 2006). In addition to the effects of their emissions on atmospheric physical and

chemical properties and climate, biomass burning interacts more broadly with the Earth's biogeochemical, hydrological, and energy cycles through a series of complex processes (Levine, 1991).

Most biomass burning occurs in the tropical regions (Brass et al., 1996; Hao & Liu, 1994), where fires are used for a variety of purposes: deforestation, shifting cultivation, fresh forage growth, agricultural residue clearing, and energy production for industrial and domestic use (Andreae, 1991; Hao & Liu, 1994; Ichoku & Ellison, 2014). Thus, many studies conducted during the last few decades have shown biomass-burning-related increases in the concentrations of O₃, CO, and other trace gases over the tropics (Andreae et al., 1988; Andreae & Merlet, 2001; Watson, Fishman, & Reichle, 1990). For instance, Shi et al. (2015) evaluated the biomass burning emissions in three tropical regions (Central and South America, Africa, and South and Southeast Asia), and their results show that vegetation burning, fuelwood combustion, and human waste burning in 2010 contributed 74% (530 Tg), 23% (170 Tg), and 3% (19 Tg) of the total CO emissions over these three regions respectively, as well as 64% (4 Tg), 32% (2 Tg), and 3% (0.2 Tg) of the total black carbon (BC) emissions. That study also indicates that Africa is the largest emitter among three tropical regions.

Africa, which is the region of interest in this study, is usually regarded as the single largest continental source of biomass burning emissions (Roberts, Wooster, & Lagoudakis, 2009). African fires burn millions of square kilometers of vegetated land every year, accounting for 30% to 50% of the total amount of emissions from global biomass burning each year (Ichoku & Ellison, 2014; Roberts et al., 2009; Roberts & Wooster, 2008). To quantify the effects of tropical biomass burning on climate, it is important to have accurate estimates of biomass burning emissions. However, due to several factors including the spatially and temporally variable nature of fires, estimations of fire emissions have large uncertainties and were recently found to differ by up to a factor of 10 among different emission inventories at the regional scale in Africa (Zhang et al., 2014). Since in situ or ground-based observations cannot provide measurements of fire emissions routinely around the globe (Ichoku, Kahn, & Chin, 2012; Roberts et al., 2009; Zhang et al., 2014), satellite remote sensing is often used as a means of analyzing and evaluating smoke emissions at regional-to-global scales (Ichoku et al., 2012). In addition, geostationary satellites have received significant attention because of their relatively high frequency of fire observations in regions over which they are located (Ichoku et al., 2012; Reid et al., 2009; Zhang et al., 2012). However, they typically observe fires at relatively coarse spatial resolutions, often resulting in significant underestimation of emissions (e.g., Roberts & Wooster, 2008). To date, existing global fire emission inventories rely on data from polar-orbiting satellite sensors such as Terra- and Aqua-Moderate Resolution Imaging Spectroradiometer (MODIS) (Darmenov & da Silva, 2013; Ichoku et al., 2008; Kaiser et al., 2012; Wiedinmyer et al., 2011). One such emission inventory is the NASA Fire Energetics and Emissions Research (FEER: <http://feer.gsfc.nasa.gov/data/emissions/>), whose current version (FEERV1.0) is based on fire radiative power (FRP) and aerosol optical depth (AOD) retrievals from MODIS (Ichoku & Ellison, 2014; Ichoku & Kaufman, 2005). However, in a single day, one MODIS sensor has only 16 pole-to-pole orbits, each covering a swath width of ~2,300 km on the ground, with significant gaps between these swaths in the equatorial region (e.g., Freeborn, Wooster, & Roberts, 2011). Furthermore, fires located under thick clouds cannot be detected from space (Justice et al., 2002; Peterson et al., 2013; Polivka et al., 2016), and MODIS fire detection sensitivity decreases toward the edge of scans where the ground pixel sizes are considerably larger than at nadir (almost a factor of 10 larger at the edge of scan, Peterson & Wang, 2013).

These observational gaps and off-nadir detection limitations in MODIS fire products result in missing and discontinuous information about fires, thereby leading to the underestimation of total biomass burning emissions in regional (Wang et al., 2006, 2013; Saide et al., 2015) and global (Reid et al., 2009) transport models. When such underestimated emission interacts with other components of an atmospheric transport and chemistry model, such as the Weather Research and Forecast model coupled with Chemistry (WRF-Chem) (Grell et al., 2005, 2011), the resulting simulated smoke-induced aerosol loading amount and distribution in the atmosphere are adversely affected (Wang et al., 2006; Zhang et al., 2014).

This paper presents an algorithm for mitigating the emission biases caused by three factors: (a) cloud cover, (b) reduction in the satellite off-nadir fire observation sensitivity, and (c) satellite observing gaps in the tropics, when using pixel-level FRP data to derive FEER emissions. As described in section 2, several past

studies have attempted to make corrections for factors (a) and/or (c) (Wiedinmyer et al., 2011), but not all three factors at the same time. We have applied and evaluated this algorithm in the Northern sub-Saharan African (NSSA) region where the biomass combustion is a large contributor to gaseous and particulate emissions during the dry season. Our previous study also based on WRF-Chem simulations and satellite data analyses showed that the intense man-made burning of grassland, cropland, shrubs, and wood in the dry season (October to March) generates large amounts of smoke particles that in some cases tend to mix with Saharan dust near the surface between the equator and 10°N, although the smoke plumes may be transported above the dust layer and can subsequently spread farther to the north and south at 700 hPa or higher altitudes (Yang et al., 2013). In addition, a sensitivity study using seven different fire emission inventories showed that smoke emissions can differ by up to a factor of 12 over NSSA, which can lead to a difference in estimates of smoke instantaneous radiative effects by a factor of 33 (Zhang et al., 2014). Hence, this study examines emission uncertainties due to the satellite-based fire detection limitations from cloud cover, off-nadir view, and orbit gaps over NSSA.

Specifically, our correction algorithm is applied and evaluated for a customized, high-resolution daily FEER emission inventory (FEERV1.0-Mp6), which was generated by multiplying the FEERV1.0 emission coefficients directly with the pixel-level MODIS collection 6 FRP product at 1 km nadir resolution. Hereafter, the FEERV1.0-Mp6 emission product prior to and after the application of the correction algorithm is called the original inventory and adjusted inventory, respectively. The emissions calculated by multiplying the ratio of total emission between adjusted and original inventory to the original inventory is named “scaled” inventory, and such scaling is done on a daily basis. Each of the three inventories was ingested into the WRF-Chem model, which was used to simulate transport of smoke particles over NSSA in January 2010 to evaluate our correction method. The evaluation is done by investigating particle loading in the atmosphere caused by biomass burning over this region. Since 5–10% of the total smoke aerosol mass is contributed by BC and 50–60% is from organic carbon (OC) (Reid et al., 2005; Tosca et al., 2014), only BC and OC from smoke particle emissions are treated as smoke emissions in this study, similar to our past work (Yang et al., 2013; Wang et al., 2013; Zhang et al., 2014). It is noted that the mass of organic particulate matter is about 40–70% more than OC mass (Wang et al., 2006). Therefore, in our WRF-Chem simulations, OC mass is multiplied by a factor of 1.7 to convert it to organic particulate matter, which, according lab data, normally makes up 80–90% of the smoke particle mass (Reid et al., 2005).

In section 2, we briefly introduce the history of fire and fire emission estimation, focusing on key uncertainties due to the inherent limitations in the polar-orbiting satellite observations. In section 3, we describe the data and model used in this study. The emission correction method and the result evaluation are described in sections 4 and 5, respectively. In section 6, we provide a summary and discussion about this work.

2. A Brief Survey of Common Uncertainty Sources in Fire Emission Estimation

Plants have been known to provide a significant amount of combustible organic matter for fires since the Silurian Period, 420 million years ago (Andreae, 1991; Bowman et al., 2009; Scott & Glasspool, 2006). The advent of grazers on the Earth altered the relatively simple relationship between plants and wildfires by their consumption of combustible material (Andreae, 1991; Schüle, 1990). After the era of dinosaur dominance and demise, the evolution of hominids caused fire frequency changes, and Earth's ecology became profoundly affected by human-caused fires used for deforestation, shifting agriculture, agricultural waste burning, cooking, and heating (Andreae, 1991; Bowman et al., 2009; Crutzen & Andreae, 1990). Measurements of charcoal and elemental carbon in sedimentary archives, while valuable for us to have as a qualitative description of the fire history on Earth (as described above), are often insufficient to establish a quantitative and robust analysis of biomass burning before the 1960s (Andreae, 1991; Andreae & Merlet, 2001; Bird & Cali, 1998; Power et al., 2008).

Darley et al. (1966) were among the earliest to conduct the pioneering work of estimating biomass burning emissions. They used a burn tower to simulate an open combustion situation at the University of California, Riverside. Their gas sampling and analysis instruments were placed in the stack of a tower to measure concentrations of hydrocarbon, CO, and CO₂. These data were then analyzed with total dry matter mass burned to derive the emission factor (EF), based on the following relationship:

$$M_s = \beta_s \cdot M_{\text{dry}} \quad (1)$$

where β_s is the EF of species s , in units of grams of s per kg of dry fuel burned for a given biome type (Andreae & Merlet, 2001); M_{dry} is the amount of dry fuel burned; and M_s is the total emission for s (Darmenov & da Silva, 2013).

Indeed, equation (1) was used in the earliest biomass burning emission studies that started from laboratory investigations of EF. In the 1960s and 1970s, such laboratory experiments were systematically used to investigate fire emissions from agricultural wastes that were burned and their corresponding EFs (Boubel, Darley, & Schuck, 1969; Darley et al., 1966; Gerstle & Kemnitz, 1967; Sandberg, Pickford, & Darley, 1975). Those studies found that EFs have high spatial and temporal variabilities, even for the same biome, and the lab measurements of EFs may not provide representative values for realistic fires (Reid et al., 2005). Thus, in the late 1970s, field measurements were gradually adopted in fire emission investigations. By collecting trace gas samples in stainless-steel containers in flights through two smoke plumes, Crutzen et al. (1979) measured and summarized the ratios of various gases to CO_2 . The emission ratios were then used to roughly estimate emission of trace gases from global biomass burning by multiplying them to the gross CO_2 amount (estimated as $2\text{--}4 \times 10^{15} \text{ g C yr}^{-1}$) (Seiler & Crutzen, 1980). This approach was followed by most of the early studies in which emission of a certain species was estimated by multiplying the corresponding EF for that species with either its known gross fuel amount or CO_2 .

Another important parameter in equation (1) is M_{dry} , which was formulated by Seiler and Crutzen (1980) as follows:

$$M_{\text{dry}} = A \cdot B \cdot C \quad (2)$$

where A is total land area burned annually ($\text{m}^2 \text{ yr}^{-1}$), B is the fuel load above the ground (g m^{-2}), and C is the fraction of the above-ground biomass that is burned (usually referred to as combustion completeness or the combustion factor). Seiler and Crutzen (1980) also summarized parameters in equation (2) from past literature for different types of biomes and estimated the global annual total dry fuel burned.

Following the development of equations (1) and (2) in the 1960s–1980s, the first monthly comprehensive database that describes the spatial distribution of global fire emission was developed by Hao and Liu (1994). Their study discovered the places with high frequency burning over the tropics and the peak burning months in different parts of the world. The study, however, relied upon ground-based reports of biomass burning amounts in tropical America, Africa, and Asia during the 1970s and was not estimated for any particular year.

Emission inventories at higher temporal resolutions (e.g., daily or hourly) were not available until the routine detection of fires from satellite was possible. While operational detection of fires from satellites started in late 1980s and early 1990s (Flannigan & Haar, 1986; Prins & Menzel, 1992; Prins & Menzel, 1994; Robinson, 1991), the first operational and global estimate of fire emissions, namely, Fire Locating and Modeling of Burning Emissions (FLAMBE), did not start until the 21st century (Reid et al., 2004). FLAMBE provides global hourly emissions with 1–5 km spatial resolution based on fire hot spot data detected by the Geostationary Operational Environmental Satellite (GOES) series and the MODIS sensors aboard the Terra and Aqua polar-orbiting satellites (Reid et al., 2004, 2005, 2009).

Further advancement in satellite remote sensing of fires also led to new ways to estimate fire emission (e.g., Darmenov & da Silva, 2013; Ichoku & Ellison, 2014; Ichoku & Kaufman, 2005; Ito & Penner, 2004; Kaiser et al., 2012; Reid et al., 2009; van der Werf et al., 2010; Wiedinmyer et al., 2011). In particular, the fire radiative energy (FRE), or integration of fire radiative power (FRP) with time, was introduced as a concept in the late 1990s, and FRP began to be retrieved from MODIS in early 2000s (Justice et al., 2002; Kaufman et al., 1998). The linear relationship between FRE and the dry fuel burned was subsequently established (Wooster, 2002):

$$M_{\text{dry}} = \alpha \cdot \text{FRE} \quad (3)$$

where α is the radiative energy combustion factor that can be derived from in situ measurements. Hence, the emission rate of species s per unit area, E_s , can be expressed as

$$E_s = \frac{\beta_s M_{\text{dry}}}{A \cdot \Delta t} = \alpha \beta_s \cdot \frac{F}{A} \quad (4)$$

Table 1

Comparisons of Different Global Smoke Emission Inventories Based on Burned Biomass Estimates From Fire-Pixel Counts and/or Burned Areas Using Satellite Data (e.g., Estimates Without Using FRP)

	FLAMBE ^a	GWEM ^b	GFED ^c	FINN ^d
Parameters				
Land cover	USGS ^e	IGBP ^h and MODIS	MODIS	IGBP ^h and MODIS
Fuel load (kg/m ²)	Reid et al. (2005) ^f	Vegetation model	Vegetation model	Literature ⁱ
Burn area (m ²)	Satellite active fire ^g	Satellite burn scar ^j	Satellite burn scar ^j	Satellite active fire ^m
EF (g/kg)	Reid et al. (2005) ^f	Andreae and Merlet (2001)	Andreae and Merlet (2001)	Literature ⁿ
Combustion completeness	Reid et al. (2005) ^f	Reid et al. (2005)	van der Werf et al. (2006) ^k	Literature ^o
Bias correction				
Swath gap	No	Yes ⁱ	Yes ^j	Yes ^g
Large VZA	No	No	No	No
Cloud cover	No	No	No	No
Reference	Reid et al. (2004, 2009)	Hoelzemann et al. (2004)	van der Werf et al. (2010, 2017)	Wiedinmyer et al. (2011)

^aFire locating and modeling of burning emissions. ^bGlobal Wildland Fire Emission Model. ^cGlobal Fire Emissions Database. ^dFire emission from NCAR.

^eUSGS 1 km AVHRR Global Land Cover Characterization (GLCC) database and classified all original 99 categories of land surface types into 10 bulk categories: bare/water, light grasses, grasslands/savannah, low woody shrub and cerrado, crops, temperate and boreal forest-low fuel load, temperate forest-high fuel load, tropical forest, wetland, and boundary regions. ^fOriginal data based on literature survey. ^gFor each MODIS-detected fire pixel, burn area of 0.63 km² is used. For GOES detected fire pixel (Prins et al., 1998), burn area is assumed to be the same as the retrieved fire size; if fire size not retrieved, 0.005 km² is used.

^hInternational Geosphere Biosphere Programme (IGBP) Land Cover Classification. ⁱThe product is at the monthly resolution based on ASTR daytime data, and ASTR nighttime active fire counts is used to adjust burn area in gap regions where burn area estimates are not available. ^jMODIS daily 500 m burn scar product is aggregated into monthly resolution at 0.25° resolution globally (Giglio et al., 2013). Monthly estimate of emission is first estimated and then distributed into daily resolution following MODIS active fire counts. While swath gaps have little effect on MODIS monthly burn scar product, it has the effect on daily resolution product, and to minimize this effect, a 3 day center mean smoothing filter is used. Furthermore, in places where fires are detected but not shown in the burn area, the detected fire counts are multiplied by the ratio between nearby burn area and the number of fire pixels in that burn area to obtain the fire area. ^kMinimum and maximum values for each fuel types are provided based on literature. These values together with moisture (and other ancillary data) are used to adjust combustion completeness for a specific month and location. ^lLiterature primarily based on the vegetation model (as in Hoelzemann et al., 2004) for each surface type.

^mFor each MODIS-detected fire pixel, 0.75 km² is assumed for grass/savannas and 1 km² for other surface types. They are further scaled accordingly to the percentage of nonbare cover in that pixel. ⁿBased on Akagi et al. (2011), Andreae and Merlet (2001), and McMeeking (2008) for each fuel type.

^oParameterize the burn area percentage for each satellite-detected fire pixel as a function of tree cover in that pixel.

where F is FRP (or $FRE/\Delta t$) that is measured from satellite in units of MW per satellite pixel, A is the area of the satellite pixel, and F/A is FRP area density (Ichoku et al., 2008). Hence, this emission rate is estimated with respect to the pixel area. Note, the product of $\alpha \cdot \beta_s$ for total particulate matter is referred to as the FRE-based emission coefficient for smoke particles or C_e (Ichoku et al., 2008; Ichoku & Ellison, 2014; Ichoku & Kaufman, 2005).

The estimates based on equations (1) and (2) are often considered as satellite estimates without using FRP, while those based on FRP or equations (3) and (4) often require the use of satellite-based FRP to estimate the total amount of biomass burned. Table 1 provides a brief description of various satellite-based emission inventories without using FRP and how each one obtains the different parameters from satellite measurements. It further shows the detailed comparison of the data sources for common parameters needed in estimates of fire emissions based on satellite observations of fire-pixel counts and/or burned area, as well as how the sampling biases caused by cloud or satellite geometry were considered in those emission inventories. The emission inventories by GWEM (Hoelzemann et al., 2004), GFED4, and FINN are estimated with special consideration of undetected fires in the satellite swath gap region. However, none of these estimates corrected the biases caused by large viewing zenith angle (VZA) and cloud cover. Table 2 lists data sources and correction of biases in some emission inventories based on MODIS FRP data. As seen from Table 2, these emission estimates were corrected for cloud cover and swath gaps (in some cases), but no correction is made for the bias due to large viewing zenith angles either.

Here we present a method to correct the emission biases introduced by (a) satellite limitations in detecting fires obscured by thick clouds, (b) low fire detection sensitivity at the edge of MODIS scans where viewing angles and MODIS pixel sizes are much larger than at nadir, and (c) data gaps between MODIS ground swaths in tropical regions. We applied this method to the pixel-level FEER BC and OC estimations at 1 km resolution in the NSSA region and evaluated its performance within the context of WRF-Chem simulations of smoke transport in this region. We note (and detailed in Appendix A) that the pixel-level FEER data (FEERv1.0-Mp6) do not make any corrections for cloud cover or swath gaps or large VZA.

Table 2

Comparisons of Different Smoke Emission Inventories Based on Satellite Fire Radiative Power (FRP) Measurements

	GFAS ^a	QFED ^a	FEER ^c	FEERv1.0-Mp6 ^d
Parameters				
FRP (W)	MODIS	MODIS	MODIS ^f	MODIS
Land cover map	Heil et al. (2010, 2012)	IGBP	FEER BB-LCT v1 ^{g,h}	FEER BB-LCT v1 ^{g,h}
EF (g/kg)	Andreae and Merlet (2001) and Christian et al. (2003)	Andreae and Merlet (2001)	Andreae and Merlet ^{g,i}	Andreae and Merlet ^{g,i}
α^i (kg/MJ)	Heil et al. (2010, 2012)	Kaiser et al. (2009)	N/A	N/A
C_e^k (kg/MJ)	N/A	N/A	FEERv1.0 C_e	FEERv1.0 C_e
Bias correction				
Swath gap	Yes	Yes	No	No
Large VZA	No	No	No	No
Cloud cover	Yes ^e	Yes ^e	Yes ^e	No
References	Kaiser et al. (2012)	Darmenov and Da Silva (2013)	Ichoku and Ellison (2014)	Ichoku and Ellison (2014)

^aGlobal Fire Assimilation System. ^bQuick Fire Emission Data Set. ^cFire Energetics and Emissions Research emission that is estimated at spatial resolution of 0.5°. ^dThis particular version of FEER is customized for this modeling study where emission is estimated at pixel level and no correction for swath gap and cloud cover is made. ^eClear-sky FRP density stands for whole grid box having the size consistent with spatial resolution of emission data product. ^fGridded based on Kaiser et al. (2012). ^gThe land cover map and EF data were used only for conversion from total particulate matter to other species and are not used as part of the core algorithm. ^hThe FEER Biomass Burning Land Cover Type product uses the IGBP classifications from the MODIS MCD12Q1 product, with consideration of fire detections from the MODIS MOD14/MYD14 active fire product. ⁱAndreae and Merlet (2001) with 2014 updates (personal communication) for converting from total particulate matter (TPM) to other species. ^j α is a conversion factor that links FRP to dry matter combustion rate. ^k C_e is a conversion factor that links FRP to particulate matter emission rate.

3. Model and Satellite Data Processing for Model Evaluation

The WRF-Chem simulations were conducted by using the FEERv1.0-Mp6 original emissions, adjusted emissions, and scaled emissions. The impact of the correction was then analyzed by comparing the simulated results with AOD data from AERONET, MODIS, and CALIPSO.

3.1. WRF-Chem Model

The WRF-Chem model (Fast et al., 2006; Grell et al., 2005), which is a fully coupled meteorology-chemistry-aerosol model, is used in this study to investigate how the method for correcting emission inventory biases due to satellite fire observation limitations may affect the simulation of atmospheric aerosol loading. The model configuration options, which are similar to those of our previous studies in the NSSA region (Yang et al., 2013; Zhang et al., 2014), are listed in Table 3. In brief, radiation schemes used in this study include the Goddard two-stream multiband scheme with ozone from climatology and cloud effects (Chou et al., 1998) for short wave and the Rapid Radiative Transfer Model (RRTM) scheme for long wave (Mlawer et al., 1997). The Regional Acid Deposition Model, version 2 (RADM2) chemical mechanism (Stockwell et al., 1990) is adopted in this study. The aerosol modules are Modal Aerosol Dynamics Model for Europe (MADE) (Ackermann et al., 1998) and Secondary Organic Aerosol Model (SORGAM) (Schell et al., 2001). We have also used the Noah Land Surface Model with soil temperature and moisture in four layers, fractional snow cover, and frozen soil physics (Chen & Dudhia, 2001) in this study. The Yonsei University (YSU) scheme (Hong et al., 2006) is selected as the boundary layer parameterization. A sophisticated microphysics scheme (Lin et al., 1983) that has ice, snow, and graupel processes, which are suitable for real-data high-resolution simulations, and the New Grell cumulus scheme (G3) (Grell & Dévényi, 2002) were also used in our model configuration.

The initial and boundary conditions for WRF-Chem model were provided by the Global Final Analysis (FNL) data from the National Centers for Environmental Prediction/National Center for Atmospheric Research (NCAR) data set. The FNL data, which include a variety of variables, are available for 00:00, 06:00, 12:00, and 18:00 UTC at 1°×1° horizontal resolution and 26 vertical levels (Kalnay et al., 1996). The FNL data used for this study has been obtained from <http://rda.ucar.edu/datasets/ds083.2/>. This study focuses on a month (January 2010) with intense biomass burning in NSSA.

The first week of the WRF-Chem simulation is set as the model spin-up time. A double-nested grid configuration of WRF-Chem is used, with the fine grid of 130×85 points and 27 km grid spacing covering NSSA

Table 3

Configuration Options Employed by WRF-Chem in This Study

Atmospheric processes	Model options
Shortwave radiation	Goddard (Chou et al., 1998)
Longwave radiation	RRTM (Mlawer et al., 1997)
Gas-phase mechanism	RADM2 (Stockwell et al., 1990)
Aerosol model	MADE/SORGAM (Schell et al., 2001)
Land surface model	Noah (Chen & Dudhia, 2001)
Boundary layer scheme	YSU (Hong, Noh, & Dudhia, 2006)
Microphysics	Lin, Farley, and Orville (1983)
Cumulus	New Grell (Grell & Dévényi, 2002)

nested within a coarse grid of 259×133 points and 81 km grid spacing. The lower left corners for these two domains are (21.88°S, 29.42°W) and (13.24°S, 16.55°W), respectively. These model domain grid settings are the same as that in our previous study (Zhang et al., 2014), and both horizontal grids use 27 vertical levels. BC and OC from the FEERV1.0-Mp6 emission inventory were used as the fire emission input into the model. As implemented in our prior study on the same domain (Yang et al., 2013), the smoke injection height was set at 650 m, such that the smoke emissions are treated as well mixed in the model layers below this injection height. No dust emission is considered in this study, and consequently, our analysis focuses on the smoke dominated region (see details in section 5).

3.2. AERONET Data

The optical ground-based Aerosol Robotic Network (AERONET), established by the National Aeronautics and Space Administration (NASA) in collaboration with a number of other organizations, has hundreds of sites distributed across the world to measure direct and sky light radiance from the Sun (Holben et al., 1998). The Sun-sky scanning radiometer at each site measures spectral radiances that are used to derive aerosol optical properties (e.g., aerosol spectral optical depth (AOD), Angstrom exponent, and aerosol size distribution) (Dubovik et al., 2000). We use AERONET cloud-screened and quality assured (Level 2.0) AOD whose uncertainty is about 0.01–0.02 (Eck et al., 1999; Levy et al., 2010). To facilitate the use of AERONET AOD as ground truth in this paper to compare with satellite and model simulation results, we used the Angstrom exponent based on AOD at 0.44 μm and 0.675 μm to interpolate AOD at 0.55 μm . Three AERONET sites that are close to the high biomass burning activity region and having valid Level 2 data in our study time period were selected in this study to evaluate MODIS AOD data. The three AERONET sites are Ilorin (8.3°N, 4.3°E), Djougou (9.8°N, 1.6°E), and Kibale (0.6°N, 30.3°E).

3.3. CALIOP Data

Cloud-Aerosol Lidar with Orthogonal Polarization (CALIOP) is a two-wavelength polarization active lidar aboard the CALIPSO satellite, launched in April 2006 (Winker et al., 2010). The data used in this study include CALIOP lidar level 2 aerosol profile products and have a horizontal resolution of 5 km and a vertical resolution of 60 m, up to 20 km. CALIOP Level 2 data were derived in two steps, first by separating the aerosol and cloud layers based on an algorithm developed by Liu et al. (2004, 2009), and then by retrieving the profiles of particle backscatter and extinction coefficients using a hybrid extinction retrieval algorithm (Liu et al., 2004, 2009; Winker et al., 2010). CALIOP extinction profile was used to evaluate WRF-Chem simulations at night, when AOD retrieval is not possible from passive remote sensing techniques.

3.4. MODIS Data, Processing Method, and AOD Evaluation

AOD, fire, and cloud products from MODIS instruments on Terra and Aqua are used in this paper. The Terra satellite (launched in 1999) passes across the Equator at 10:30 a.m. local time, and the Aqua satellite (launched in 2002) at 1:30 p.m. Active fire products from MODIS are based on the algorithm that uses brightness temperature measurements at 3.96 μm and 11.0 μm wavelengths to detect active fires and other thermal anomalies (Giglio, 2010; Justice et al., 2002). Each MODIS Level 2 fire product granule covers a region of approximately $2,340 \times 2,030$ km in the along-scan and along-track directions, respectively. It has a 1 km resolution at nadir and contains the FRP and flags that identify fires and other relevant pixels (Giglio, 2010). MODIS Level 2 daily cloud product, MOD/MYD_06 (Ackerman et al., 1998; Platnick et al., 2017), from the Terra and Aqua satellites is also used in this paper for MODIS AOD quality control and in the emission correction algorithm. MOD/MYD_06 products provide cloud fraction at 1 km resolution.

MODIS AOD data are retrieved over land at 0.47, 0.55, 0.66, and 2.13 μm wavelengths and over ocean at 0.48, 0.55, 0.66, 0.87, 1.20, 1.60, and 2.13 μm . The newest MODIS Collection 6 (C6) aerosol products have three parts: (1) "Dark Target" (DT) over ocean, (2) DT over vegetated or otherwise dark land surfaces, and (3) "Deep Blue" (DB) over bright land surfaces (Levy et al., 2013). For MODIS-retrieved C6 AOD (at 0.55 μm) from the DT algorithm, the expected error is $\pm(0.03 + 5\%)$ over ocean and $\pm(0.05 + 15\%)$ over land (Levy et al., 2010, 2013; Remer et al., 2008). The highest quality AOD (at 0.55 μm) from the DB algorithm has an absolute uncertainty of $0.03 + 20\%$ (Sayer et al., 2013). In this study, we use both Terra (MOD_04) and Aqua (MYD_04) C6 AOD data at 0.55 μm wavelength and 10 km spatial resolution to evaluate the model performance resulting from applying the emission correction method.

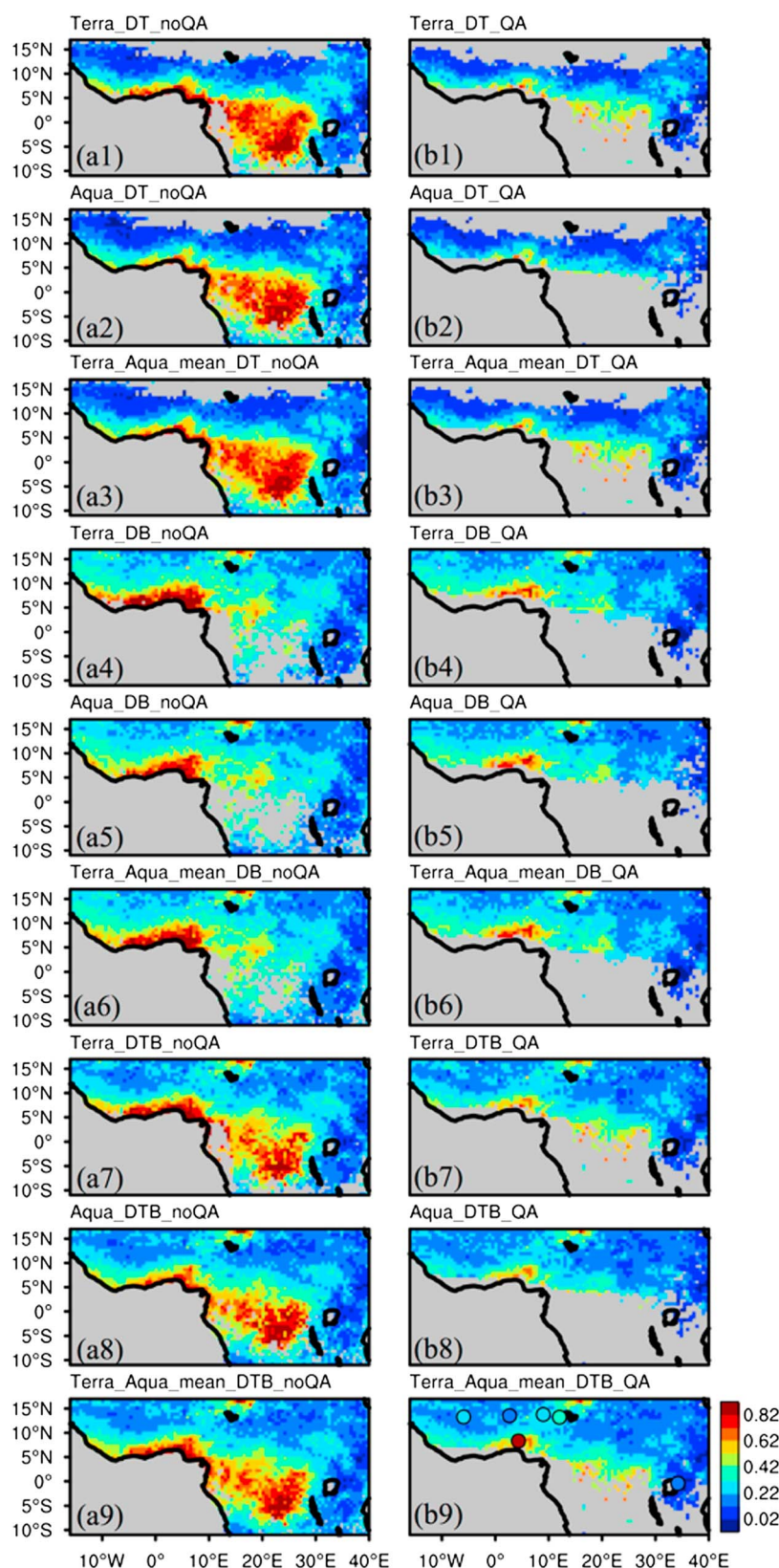


Figure 1. (a1–a9): Monthly Terra DT, Aqua DT, Terra Aqua Mean DT, Terra DB, Aqua DB, Terra Aqua DB, Terra DTB, Aqua DTB, and Terra Aqua DTB AOD at 0.55 μm before QA in January 2010. (b1–b9) are similar to Figures 1a1–1a9 but for AODs after QA. The filled circles in Figure 1b9 indicate AERONET monthly average AOD at 0.55 μm .

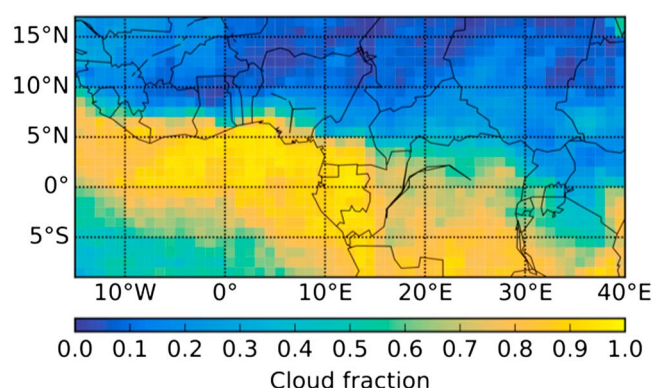


Figure 2. Distribution of cloud fraction averaged in January 2010, based on MODIS/Terra day-time cloud products (MOD08, collection 6, Platnick et al., 2017).

Since our current emission correction method aims at the NSSA land region, only MODIS land AOD is used in this paper to evaluate the impact of our emission correction on the WRF-Chem simulation of AOD. Several quality assurance (QA) filters are used in this work to reduce DT and DB AOD errors, including the use of QA flags, body checks (for smoothness), and removal of AOD retrieved at large scattering angles (Hyer, Reid, & Zhang, 2011; Vermote & Roy, 2002; Zhang & Reid, 2006). DB data QA processing is similar to that of DT (Shi et al., 2013).

Averages of DT and DB AOD are also calculated and defined as “DTB” in this study. Figure 1 shows the monthly average of Terra DT, Aqua DT, Terra and Aqua mean DT, Terra DB, Aqua DB, Terra and Aqua mean DB, Terra DTB, Aqua DTB, and Terra and Aqua mean DTB AOD at 0.55 μm before and after applying the QA filtering procedures. AERONET monthly AOD values at six stations in the study region are

also overlaid in Figure 1b9. AERONET daily average data are computed for days that have two or more observations. The monthly average of MODIS AOD is then calculated when the number of days with valid data is greater than 5 in that month. Before QA, Terra MODIS AOD tends to be higher than Aqua MODIS AOD between 2°N and 11°N. The QA process removed 20–30% of data points in the study region no matter which group of AOD was checked, particularly along the coastal and dense tropical forest regions. The removal of high AOD along the coast is primarily due to low QA assurance in the MODIS products. Since we lack AERONET sites along the coast, it is challenging to determine whether some QA flags in MODIS products can be universally applied, although our past study has shown that MODIS DT retrieval over coastal regions overall has larger uncertainties than either over the open ocean or in-land areas (Anderson et al., 2013). Furthermore, the removal of high AOD values below 5°N and the coast is likely due to cloud contamination. Clouds are persistent in the regions centered around (2.5°S, 30°E), as we can see from Figures 1a and 1b (true color images), and indeed, the cloud fraction as retrieved from MODIS is in the range of 60–100% in these regions (Figure 2). Nevertheless, a high AOD zone with significant contributions from the biomass burning region is prominent on the map (0°–10°N). The monthly average AERONET AOD is consistent with MODIS AOD outside of the burning region, whereas at the Ilorin station (which is closest to the intense biomass burning region), it is higher than the monthly MODIS AOD. Further checks show that the AERONET site in Ilorin only has 2 days of valid AOD data at level 2, but 17 days of valid AOD data at level 1.5, suggesting that this is a site that also has high cloud contamination, consistent with MODIS cloud fraction data (Figure 2).

Given the large spread of MODIS AOD between different algorithms and their combinations for January 2010, we further evaluated the MODIS AOD data before and after QA procedures using the available 2003–2016 January AERONET data. The satellite and AERONET collocation follows the spatiotemporal method proposed by Ichoku et al. (2002). The collocated data statistics are calculated only when there are at least five valid AOD data points from MODIS and two valid data points of possibly four to five AERONET data points within ± 30 min (Levy et al., 2010). Figure 3 shows that, for different group comparisons, the MODIS AOD overall has better correlation and smaller RMSE after QA. Based on the results in Figure 3, we decided that Terra and Aqua DB mean AOD after QA filtering are most suited for evaluating the model performance over NSSA in January 2010 because, when compared to other groups, it (Figure 1b6) has one of the highest correlations and the lowest RMSE with respect to AERONET AOD. Furthermore, to enable data evaluation at Aqua gaps and large VZA regions, Terra AOD is also required. Terra DB after QA is selected as “truth” data for model evaluation at Aqua gaps and large VZA regions because of its relatively low RMSE and high correlation compared to the other Terra groups.

4. Emission Data Processing and Correction

Figure 4 shows the flowchart of our emission correction method. First, the FEERV1.0-Mp6 pixel-level (1 km) data were lumped into four groups: (1) Terra daytime, (2) Terra nighttime, (3) Aqua daytime, and (4) Aqua nighttime, and the corresponding emission data are summed for each WRF-Chem gridbox, following the gridding procedure by Kaiser et al. (2012). Second, a two-step correction approach is used to update the

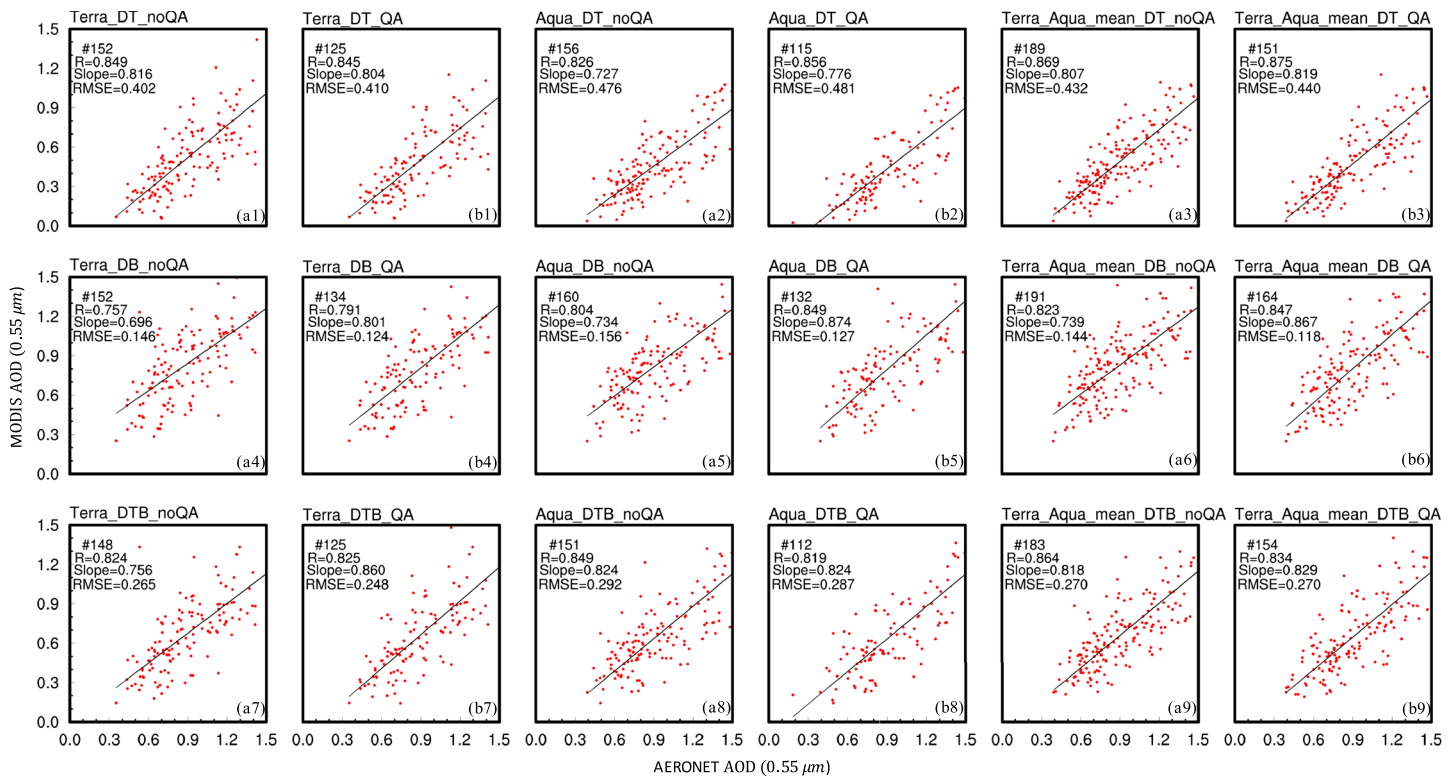


Figure 3. Regional comparisons between daily MODIS AOD and AERONET AOD at 0.55 μm . (a1–a9) Terra DT, Aqua DT, Terra Aqua Mean DT, Terra DB, Aqua DB, Terra Aqua DB, Terra DTB, Aqua DTB, and Terra Aqua DTB AOD before QA; (b1–b9) MODIS AOD after QA.

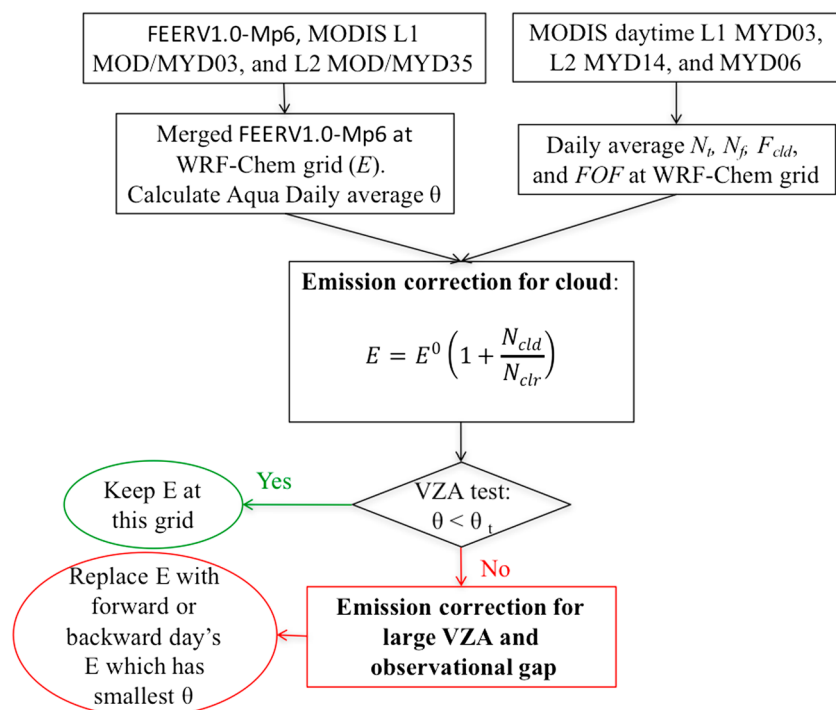


Figure 4. Flowchart of emission bias correction method.

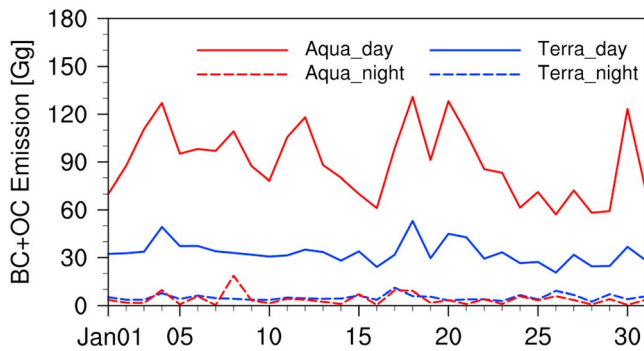


Figure 5. Time series of inner domain total BC + OC emission respectively from MODIS Terra and Aqua for either day or night.

baseline emissions, as described below, one for correcting the cloud effect and another for the large view-angle effect and satellite orbital gaps. As shown in the time series of BC and OC original emissions from the aforementioned four groups (Figure 5), Aqua daytime consistently shows the largest emission on a day-to-day basis, producing a daily-mean emission value of 89.82 Gg, which differs significantly with the daily-mean emissions from Aqua nighttime, Terra daytime, and Terra nighttime of 3.98, 33.02, and 5.10 Gg, respectively. Thus, for simplicity, the two-step correction approach is illustrated below by using Aqua daytime observations only.

4.1. Emission Correction for Cloud

The assumption in the emission correction for the cloud effect is that at each WRF-Chem gridbox (27 km), the spatial distribution function of fire emission or fraction of fire (FOF) is the same between cloudy and cloud-free areas under similar conditions (Cardoso et al., 2003; Darmenov & da Silva, 2013; Giglio, Csiszar, & Justice, 2006; Giglio, Kendall, & Mack, 2003; Heald et al., 2003; Roberts et al., 2005; Robinson, 1991; Schroeder, Csiszar, & Morissette, 2008). While this assumption may lead to the possibility of overestimating emission if fires are prone to occur over cloud-free conditions, no fire data underneath the clouds are available to evaluate this possibility, and furthermore, this assumption is only applied at the gridbox level. In other words, the uncertainties from this assumption are only limited at these gridboxes that, according to MODIS data, are partially cloudy and have fire pixels. With this assumption, the amount of emission estimated by FEER in cloud-free conditions can be used to estimate emission under cloudy conditions, after the FOF is computed from fire pixel counts (N_f), the number of pixels obscured by clouds (N_{cld}), and the total number of nonwater MODIS pixels (N_t).

$$FOF = \frac{N_f}{N_t - N_{cld}} = \frac{N_f}{N_{clr}} \quad (5)$$

where N_{clr} is the number of nonwater cloud-free (or clear-sky pixels). The MODIS L2 MOD/MYD35 cloud mask products are used to derive N_t and N_{cld} , while the active fire product is used to derive N_f . Consequently, for the WRF-Chem grid, the new emission after the correction for cloud is

$$E = E^0 + E^0 \left(\frac{N_{cld} \cdot FOF}{N_f} \right) = E^0 \left(1 + \frac{N_{cld}}{N_{clr}} \right) \quad (6)$$

In (4), E^0 is the original emission at WRF-Chem grid, E is the new emission after cloud correction, and N_{clr} is the number of clear-sky nonwater pixels (or the difference between N_t and N_{cld}) by MODIS.

4.2. Emission Correction for Large View Angle and Gap Filling

To illustrate the view angle effect on fire detection and emission estimates, we show in Figure 6 the Aqua-MODIS true color image overlaid with the satellite detected daytime fires (red dots), and Terra Aqua mean DB AOD, on 1 and 2 January 2010. The white solid, dotted, and dashed lines in Figures 6c and 6d stand for Aqua swath borders, ground boundaries for viewing angle $\theta = 35^\circ$, and center (nadir) of the satellite view. On 1 January, regions with $\theta > 35^\circ$ have much fewer fire pixels detected by satellite (yellow boxes in Figure 6a), although the AOD retrievals reveal that nearly the same amount of smoke AOD exists in the scan-edge regions as in the nadir views (Figure 6c); similar mismatch can also be found on 2 January (e.g., for the region marked as red box in Figures 6b and 6d). In contrast, the fire density in the same region (of yellow box with low number of fire pixels) is clearly higher on 2 January when MODIS provides a nadir view for this region (Figure 6b). Such contrast can be found routinely in the analysis of satellite fire products and thus needs to be corrected. Furthermore, as marked in Figure 6a, there is no fire information at the gap between the two continuous ground tracks of MODIS Aqua observation. Yet even within the same day, valid and large AOD retrievals from MODIS Terra can be found in these Aqua gap regions, suggesting a high probability of fires in these gap regions (Figure 6a versus Figure 6c for yellow box). A previous study based on SEVIRI FRP data records over Africa at 15 min temporal interval (Roberts et al., 2009) also suggests that such apparent absence of fires at MODIS swath gaps and off-nadir regions, and presence of fires the next day when the gap moves to a different location, is not authentic. Hence, from fire emission point of view, the swath gaps and the regions having large VZAs should and are treated similarly in our correction approach.

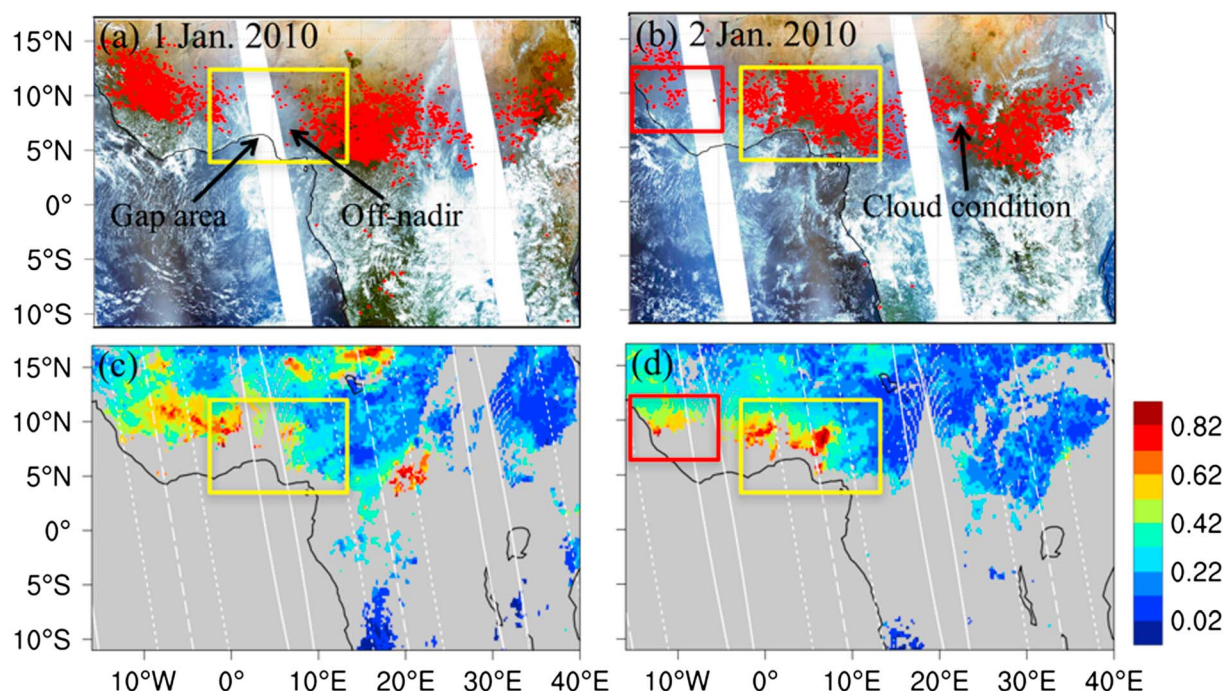


Figure 6. (a and b) Aqua MODIS true color image overlaid with daytime fires (red dots) on 1 and 2 January 2010. (c and d) MODIS Terra and Aqua DB mean AOD after QA at $0.55 \mu\text{m}$ on the same days as Figures 6a and 6b. The white solid, dot, and dash lines in Figures 6c and 6d stand for Aqua swath borders, Aqua boundaries for $\theta = 35^\circ$, and the center (nadir) of satellite observations. The rectangle in yellow shows an example of swath gap and large VZA regions on 1 January 2010; the same region is large AOD and fire pixels on the next day. The rectangle in red shows an example of the regions where large AOD is retrieved and only few fire pixels are detected.

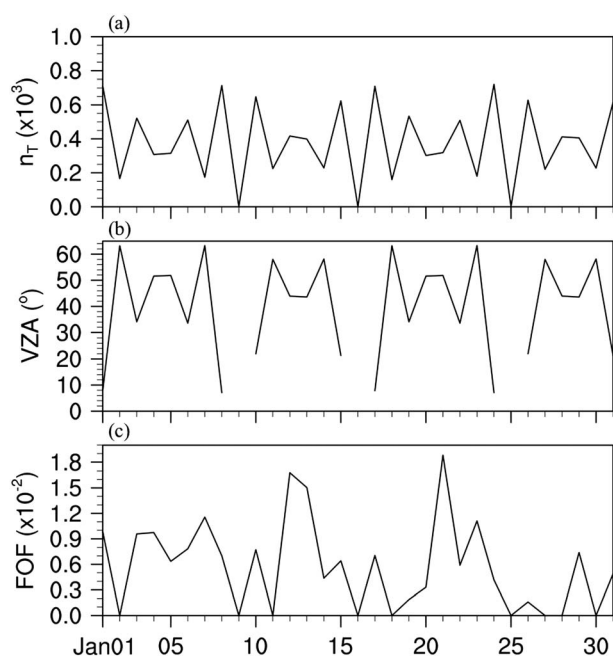


Figure 7. Time series of (a) Aqua total pixel number (N_t), (b) daytime averaged view zenith angle (VZA), and (c) the fraction of fire (FOF) in a model grid at NSSA in January 2010 for a WRF-Chem gridbox. See text for details.

The bias caused by viewing angle on fire detection is also exemplified in Figure 7 showing the time series of (a) Aqua total pixel count (N_t), (b) daytime averaged VZA, and (c) the fraction of fire (FOF) in an arbitrary WRF-Chem grid (9.0°N , 9.4°W) over NSSA in January of 2010. As expected, when the VZA increases, the total pixel count can decrease rapidly, which also affects the FOF calculation. Due to this decrease in the total number of pixels toward the edge of swath, high FOF values may occur when VZA values are relatively large. For example, as shown in Figure 7, the three largest FOF values (up to 0.018) occur when VZA is larger than 40° , which apparently is not realistic. It is understood that when VZA increases, MODIS sensitivity to small fires rapidly decreases (Peterson & Wang, 2013) and the total number of pixels (within a WRF-Chem gridbox) also decreases (and in some cases, at a much faster rate), which explains why in some cases with large VZAs, unrealistic FOF can be found (and should be corrected).

To correct the viewing angle effect on the low bias in fire emission estimation, we need to select a threshold value below which the fire detection is relatively less sensitive to the view angle. From our analysis in Figure 7 above and Figure 8 below, this threshold, θ_t , is empirically defined as 35° . Selection of θ_t requires consideration of the satellite revisit time, the accuracy of fire detection, and fire persistence. Figure 8 clearly shows that the pixel size increases and the sensitivity for detecting fires decrease within a factor of two when VZA changes from nadir to 40° (pixel area changes from 1 to 2 km^2). But, from 40° to 65° , the pixel size increases and the sensitivity of fire detection decreases by up to a factor of 6–9 (as compared to the nadir).

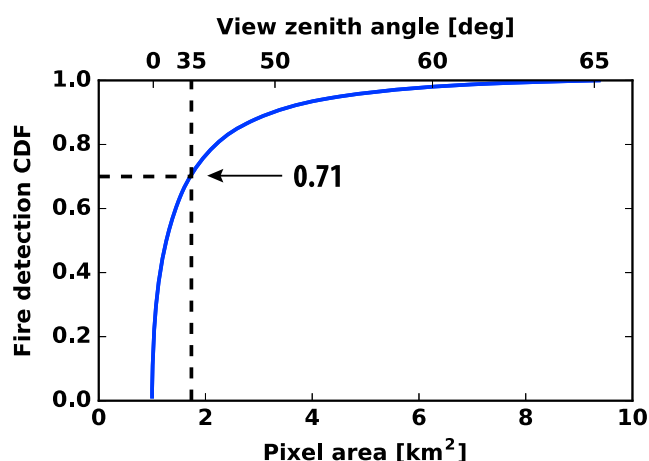


Figure 8. Cumulative density function (CDF) of MODIS-detected number of fire counts as a function of pixel area (bottom x axis) and view zenith angle (top x axis). Note, to correspond to the bottom x axis scale that is linear, the top x axis is not in linear scale.

Therefore, selecting θ_t below 40° can significantly reduce the uncertainty in emission estimation. Ideally, it would be best to completely eliminate such large uncertainties resulting from off-nadir observations, which would require using only pixels that are as close to nadir as possible. However, if we select only near-nadir observations (say for VZA less than 5°), we would need to assume fire persistence of more than 5–8 days to be able to update the emissions for a given region (because MODIS's repeat cycle is 14 days). Incidentally, 5–8 days of persistence is not realistic for agricultural fires, as previous studies have shown that agriculture fires normally last for 1–2 days (Kauffman et al., 2003). To balance these factors—fire detection sensitivity, MODIS revisit time, and the realistic number of fire persistence days—it is clear that VZA of 35° is a reasonable threshold that enables us to have consistent fire detection data to update the emissions within ± 2 days. Indeed, 71% of MODIS-detected fire pixels have VZA less than 35° or pixel area less than 1.7 km^2 (Figure 8). The assumption of a 2 day fire persistence is also consistent with a 3 day center mean smoothing used in GFED to avoid swath gaps (van der Werf et al., 2010). Future satellite fire observation from geostationary satellites that provide similar spa-

tial resolutions (of $\sim 1 \text{ km}$) to MODIS at hourly to subhourly temporal frequencies (such as GOES-R over the U.S., Schmit et al., 2016) can help us further address the issues related to the MODIS fire detection accuracy as a function of VZA and fire persistence.

Consistent with the above reasoning, for any gridbox with $\theta > \theta_t$ (including swath gaps), we replace the current emission E of this gridbox with that corresponding to the smallest VZA observed at the same location within ± 2 days; otherwise, no correction is made for view angle effects. This does not necessarily assume the persistence of the same fire for several days, since the fires in our region are typically small man-made fires (e.g., Ichoku et al., 2016). Rather, it assumes persistence in burn patterns within homogeneous local areas/villages, as each 1 km MODIS pixel likely contains several small fires.

5. Evaluation of Emission Correction for WRF-Chem Simulation

We evaluate our emission correction approach by applying the following three sets of emissions into the WRF-Chem simulation of smoke transport for January 2010: (a) the original emission, (b) the adjusted emission, and (c) the scaled emissions. The difference between using (a) and (b) in simulations of smoke transport can reveal the impact of correcting for the effect of view angle on fire observation. To avoid cases where dust may make a significant contribution to the columnar AOD (Yang et al., 2013), we restrict our analysis to the $0\text{--}10^\circ\text{N}$ latitude band, where biomass burning is most highly concentrated within our domain. Furthermore, we only conducted the intercomparison between modeled and satellite-retrieved AOD in regions where Angstrom exponent of the AOD retrieved by MODIS is larger than 1.2, to ensure that the aerosols are dominated by smoke particles.

In Figure 9 we first show the modeling results and evaluation on the same days as in Figure 6. The adjusted emission distribution corresponds well with the smoke locations observed from satellite true color imagery (Figures 6a and 6b). It clearly shows that the data gaps at the Aqua-MODIS off-nadir regions have been filled in the adjusted emission, whereas the scaled emission simply increased the total emission amount with the same relative spatial distributions as the original one. The total BC + OC emission amounts in the study region increased from 41 (40) Gg to 92 (82) Gg for 1 (2) January 2010. In the scaled emission case, while the total emission amounts increased to the same values as in the new case, the agreement between simulated (Figure 9) and MODIS AOD distribution (Figure 6) is not as good as the agreement between those simulations with adjusted emission and MODIS AOD distribution. The AOD simulated with the adjusted emission has an improved spatial pattern and reduced biases in satellite off-nadir and swath gap regions.

Quantitatively, based on the 2 day simulation results, Taylor diagrams in Figure 10 show how the emission correction method improves WRF-Chem simulated AOD. The centered root-mean-square (RMS) difference (normalized with respect to the standard deviation of observation) between WRF-Chem and MODIS AOD

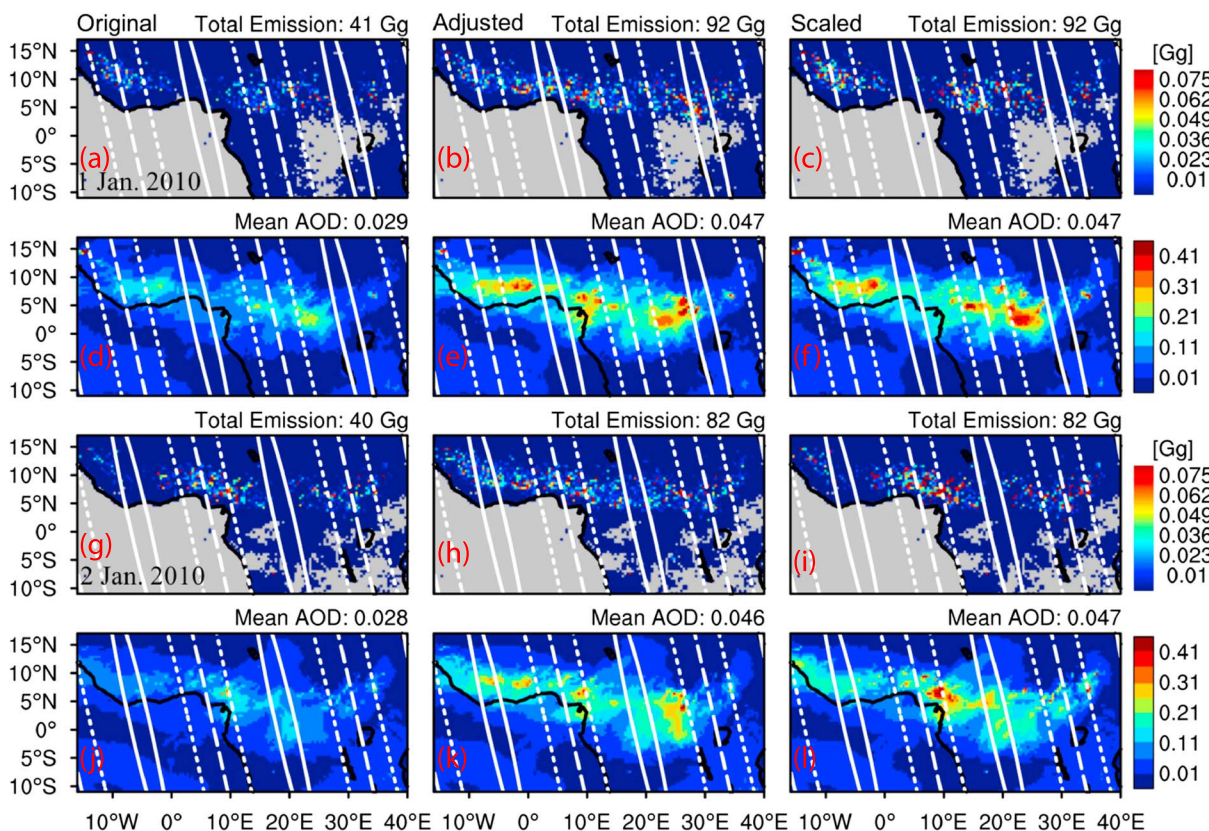


Figure 9. (a–c) Original, adjusted, scaled BC + OC emission on 1 January 2010 at WRF-Chem grid. (d–f) WRF-Chem simulated column total AOD at $0.55 \mu\text{m}$ using the emission of Figures 9a–9c during Aqua pass period (12:00–14:00 UTC). (g–i) Same as Figures 9a–9f but for 2 January 2010. The white solid, dot, and dash lines in Figures 9c and 9d stand for Aqua swath borders, Aqua boundaries for $\theta = 35^\circ$, and the center (nadir) of satellite observations.

is proportional to the distance to the point on the x axis identified as “REF” in Figure 10. “REF” is our reference or “true value” (MODIS retrievals in the present case). When using the simulated daily AOD (averaged for 08:00–20:00) compared with MODIS (Terra and Aqua) mean DB AOD over NSSA’s high fire-frequency region (0° – 10°N), the case with adjusted emission has reduced the center RMS error and standard deviation difference and increased the correlation. The scaled emission case only resulted in closer standard deviation values to the MODIS retrievals.

Further assessment of our emission correction approach for WRF-Chem simulation is conducted for the whole month of January 2010. Figure 11 shows the monthly (January 2010) average column total AOD at $0.55 \mu\text{m}$ simulated by WRF-Chem using the three (original, adjusted, and scaled) emissions. Though the overall simulated AOD magnitude (based on the adjusted emission) is smaller over the study domain (as compared to MODIS AOD), the new simulated AOD pattern clearly shows improvements in some regions relative to the scaled emission case. When compared with monthly Terra and Aqua mean DB AOD (Figure 1b6), the simulation using the adjusted emissions captures the relatively high AOD pattern in the regions marked as yellow box in Figure 6. The low bias of simulated AOD (even after the emission adjustment) is likely in part due to (a factor of two or larger) uncertainties from other sources (see Table 2).

The adjusted emission improvements to the model performance are further shown in the Taylor diagrams in Figure 12. WRF-Chem simulated daily column total AOD values at $0.55 \mu\text{m}$ are compared with Terra and Aqua mean DB after QA in Figure 10a for all VZA, and the results are shown in Figure 12a, while only a similar comparison at Aqua regions with $\theta > \theta_t$ (including gap regions) is shown in Figure 12b. In both cases, the simulation results are better than the one with the original emission, in terms of correlation, centered RMS error, and normalized data standard deviation. By comparing the adjusted results with the scaled results, we find that the model performance improvement was not simply caused by increased emission amounts but also resulted from spatial filling of the emission inventory. Indeed, in these gap-filled and large VZA regions,

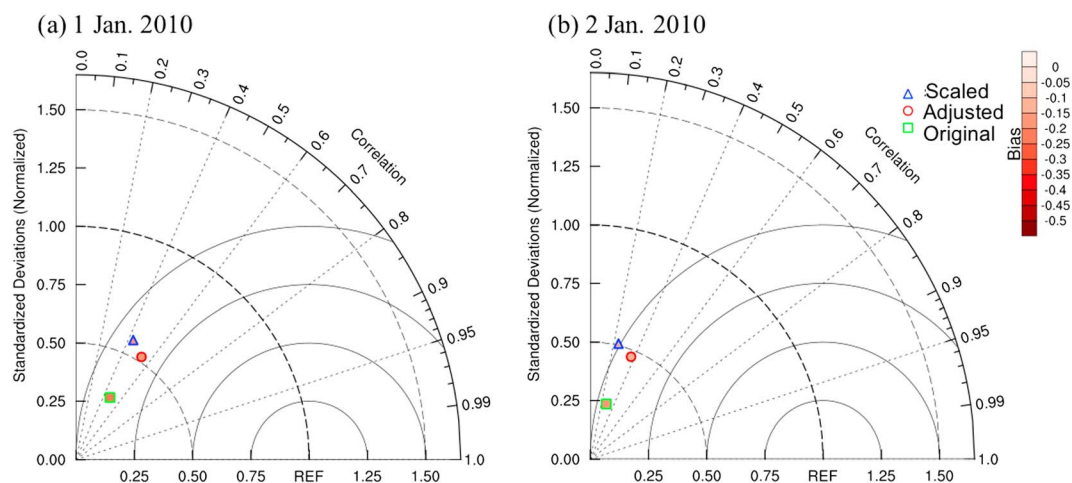


Figure 10. Taylor diagram for WRF-Chem simulated column total AOD at 0.55 μm compared with Terra and Aqua mean DB after QA in (a) 1 and (b) 2 January and 2010 over high smoke loading region. REF represents the MODIS observations. The colors filled in symbols indicate the biases between model and MODIS.

over half of the cases based on adjusted emission data are better than the scaled results. Figures 12c and 12d further show the comparison of WRF-Chem column total AOD at 0.55 μm in the whole month of January with Terra/Aqua mean AOD after QA over the heavy smoke loading zone ($0\text{--}10^\circ\text{N}$) and over regions with $\theta > \theta_t$, respectively. Overall, the adjusted emission has increased WRF-Chem simulation in aerosol loading when compared with the original and scaled cases. Using the original case as the reference, the correlation is improved from ~ 0.42 to 0.6, centered RMS error reduced from 1 to 0.7 (or $\sim 30\%$), and the normalized data standard deviation increased from 0.5 to 0.75 or a 50% improvement (Figures 12c and 12d).

To further investigate the emission correction improvements, the model results were evaluated using Cloud-Aerosol Lidar and Infrared Pathfinder Satellite Observations (CALIPSO) Cloud-Aerosol Lidar with Orthogonal Polarization (CALIOP) 5 km aerosol extinction products. Nighttime CALIOP data for three different dates were selected to represent situations when CALIPSO overpasses the same day's Aqua daytime gap and $\theta > \theta_t$ regions. Since our emission correction methods focus on this area, the vertical profile comparison is necessary to evaluate how the changes of daytime emission affect the nighttime model simulations.

Figure 13 shows the comparison of nighttime CALIOP-derived vertical profiles of aerosol extinction coefficient at 532 nm (second row) and WRF-Chem simulated vertical profiles of smoke concentration along the corresponding CALIPSO ground track using the original (third row), adjusted (fourth row), and scaled emissions (fifth row). Data for the 3rd, 4th, and 22nd of January 2010 are represented on the first to the third column. Due to cloud cover, the lidar signal was heavily attenuated over some regions. All of the three model simulated results using different emissions roughly capture the patterns of vertical aerosol profiles. The smoke particles can reach altitudes of 3 to 6 km. It is noted that the scaled emission has no effect on the aerosol vertical distribution changes but simply increases the aerosol amount on the basis of the original case. The red ovals in Figures 13a1, 13b1, and 13c1 indicate where the adjusted emission input changed the model

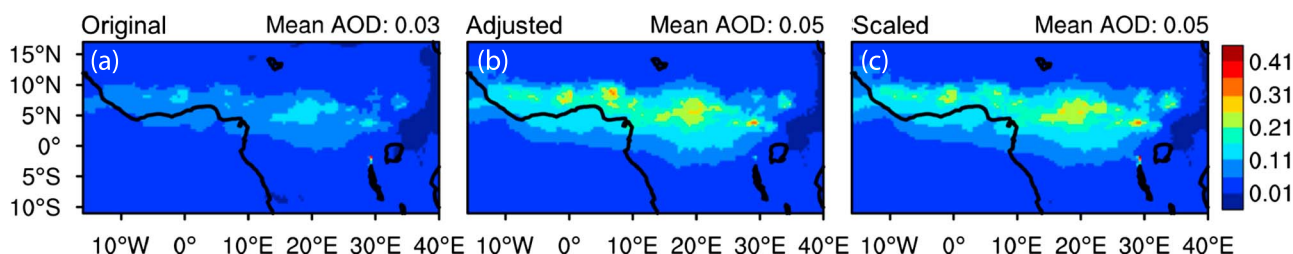


Figure 11. Monthly average WRF-Chem simulated column total AOD at 0.55 μm during daytime (08:00–20:00 UTC) using (a) original, (b) adjusted, and (c) scaled emissions for January 2010.

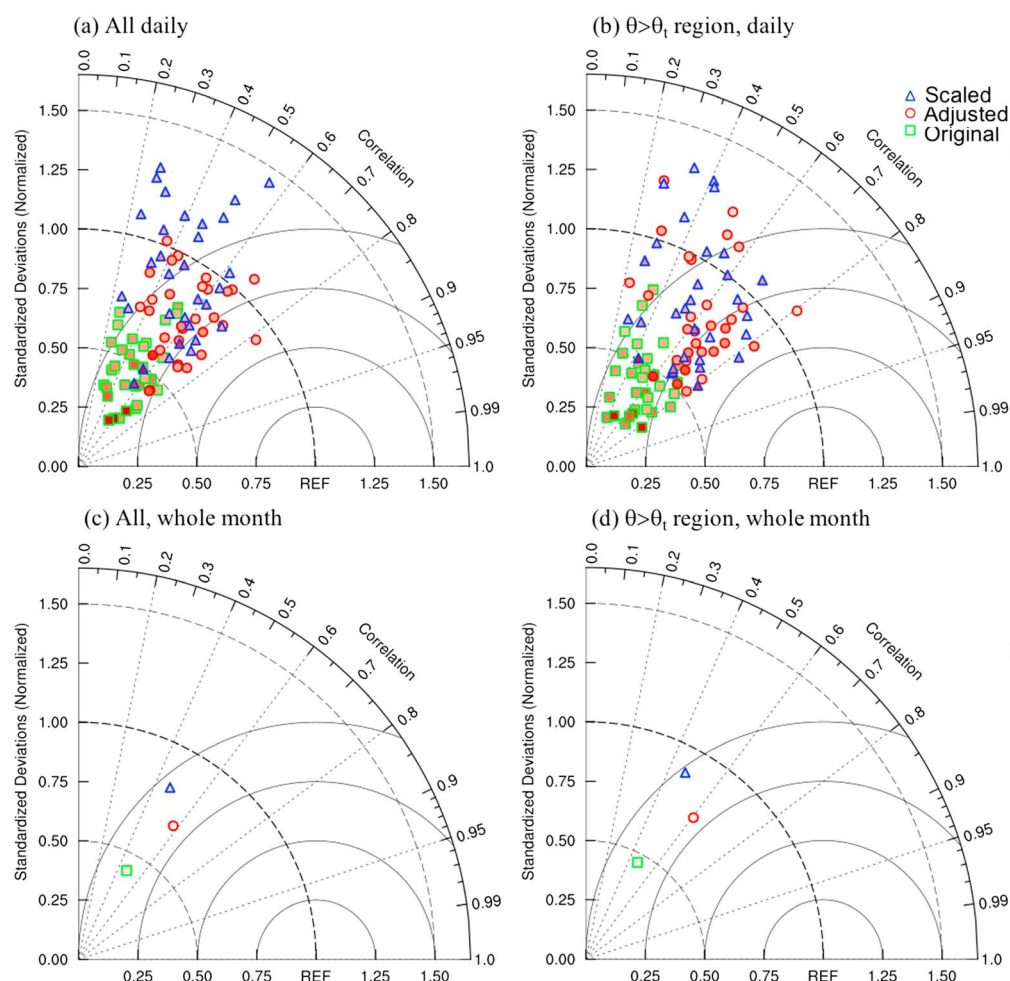


Figure 12. Taylor diagram for WRF-Chem simulated daily column total AOD at $0.55 \mu\text{m}$ compared with (a) Terra Aqua mean DB after QA within areas of high smoke loading and (b) WRF-Chem AOD compared with Terra DB AOD after QA for cases in Aqua swath gap region and the region with Aqua $\theta > \theta_t$ within high smoke loading regions. Analysis is for January 2010. REF is MODIS observation. The colors filled in symbols indicate the biases between model and MODIS. (c and d) Similar to Figures 12a and 12b but for the statistics of the entire month.

simulated aerosol vertical distributions along the CALIPSO path, showing that such change is not simply due to scaling by a fixed factor (as in the case of scaled emissions). We also checked depolarization ratio measured by CALIPSO and found that the particles in the regions marked with red ovals are overwhelmingly spherical (with nearly zero depolarization ratio). Yang et al. (2013) also showed that in cases where dust and smoke do mix together, such mixing often occurs near the surface. Therefore, aerosol particles above 2 km are dominated by smoke particles. On 3 January 2010, the aerosol extinction coefficient values marked by the red oval region are around 0.25 in Figure 13a1. The aerosol extinction coefficient data range is very similar to the values on the left side of the red oval in the figure. The adjusted emission has increased the simulated aerosol vertical loading over this region, and the magnitude is close to the aerosol concentration on the left side of the red oval in the figure. However, the simulated aerosol concentrations based on the original and scaled emissions are relatively low when compared with the results based on the adjusted emission. The model enhancement from the adjusted emission is further shown in the case of 4 January 2010. There are high extinction coefficient values over the red oval of Figure 13b1. Neither the original nor scaled simulations depict these high aerosol concentrations. Only the simulations with the adjusted emission capture the high aerosol loading over this region. A similar situation happened on 22 January 2010. The red oval in Figure 13c1 shows the center with a relatively high extinction coefficient that is only captured by the simulation using the adjusted emission.

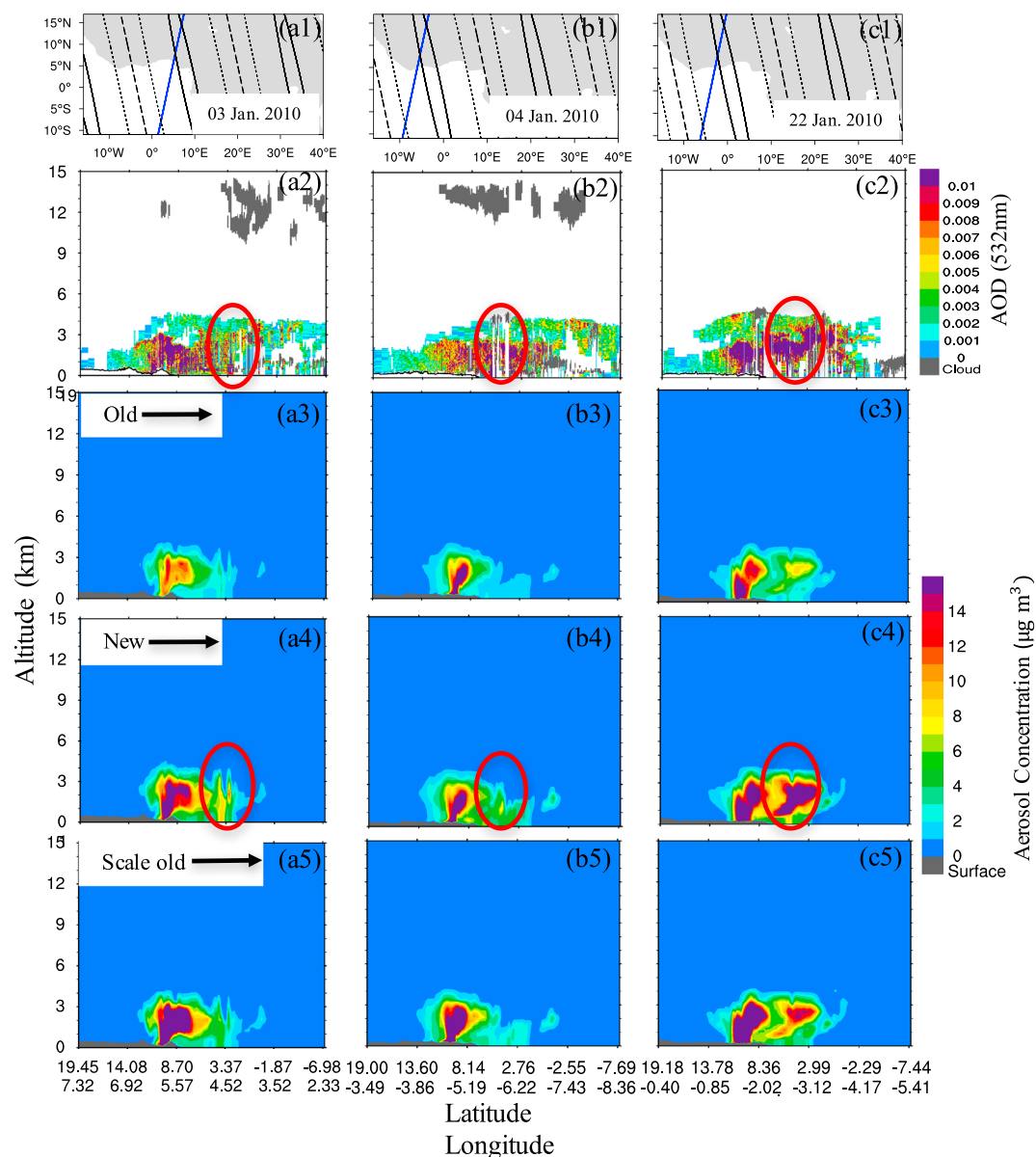


Figure 13. The first row shows selected nighttime CALIPSO tracks (blue lines) that pass over daytime Aqua large VZA or gap regions (Aqua orbits are also shown in the map, and the meaning of different line types is the same as in Figures 5b and 5c). Comparison of nighttime CALIPSO-derived AOD vertical profile (calculated from aerosol extinction coefficient) at 532 nm (second row) and WRF-Chem simulated vertical profiles of smoke concentration along the corresponding CALIPSO ground track using original (third row), adjusted (fourth row), and scaled emissions (fifth row). Data in 3, 4, and 22 of January 2010 are shown from the first column to the third column. The red ovals in the second and fourth rows show the CALIPSO-derived aerosol loading patterns captured by model simulations with adjusted emission.

6. Discussion and Conclusion

We developed a correction algorithm for improving a customizable fire emission that is based on pixel-level FRP data (FEERv1.0-Mp6) to account for some of the limitations in MODIS fire observations. Our initial analysis had indicated biases in these data caused by three satellite fire detection limitations: (a) nondetection of fires due to cloud cover, (b) the reduced sensitivity of MODIS fire detection off-nadir, and (c) the gaps between successive MODIS swaths near the equator. These three biases were compensated for in our study to generate a new spatially continuous emission inventory.

The original and adjusted inventories were applied to the WRF-Chem model to simulate smoke loading in the atmosphere. This study was conducted over NSSA during a high fire month, January 2010. The comparison with MODIS AOD revealed that the adjusted emission led to an overall improvement in WRF-Chem simulated spatial and temporal distribution of AOD in the study region. Both the daily and monthly mean simulated values were evaluated in our study using satellite observations from MODIS and CALIOP. After applying the emission correction, the emission amount increased because missing emission values were filled in regions under cloud cover, regions at large satellite scan angles, and swath gaps. The effect of this emission correction method for improving model performance was also compared with another model simulation using scaled emissions. The scaled emission has simply increased the original emission amounts based on the daily ratio of the adjusted and original emissions. Comparisons with aerosol observations at daily and monthly time scales show that simply increasing emission amounts is not enough to reduce satellite fire detection biases. There is an improvement in standard deviation and correlation when comparing the scaled results with MODIS. Overall, compared to the simulations using the original emission, the corrected (or adjusted) emission improved the WRF-Chem simulations in terms of agreement with MODIS AOD; the linear correlation coefficient (with MODIS AOD) increased by 0.18 (from 0.42 to 0.6), the centered RMS error reduced by 30% (from 1 to 0.7), and the modeled data standard deviation moved closer to that of the observed AOD by 50% (i.e., change from 0.5 to 0.75 in normalized standard deviation). The model improvement from the emission correction is also apparent by comparing nighttime CALIOP extinction coefficients at 532 nm with model simulated vertical aerosol loading along CALIPSO tracks when the CALIPSO overpasses are matched with the same day's Aqua large VZA or gap regions.

Reducing uncertainties of biomass burning emission is crucial to the reliability of model simulations of atmospheric aerosol physical properties (Zhang et al., 2014). The case study here presents a simple approach for improving emissions based on pixel-level FRP data from a polar-orbiting satellite-based fire detection algorithm that has inherent limitations in characterizing fires in cloudy conditions and at the edge of or gap areas between satellite ground swaths. With the launch of GOES-R and Himawari (Schmit et al., 2016), detection of fires at high temporal resolution from geostationary satellite sensors at similar spatial resolutions as MODIS is becoming operationally available and can be used in future studies to evaluate the empirical method developed in this paper, thereby further reducing the uncertainties due to the inherent limitations in fire detection from polar-orbiting satellites.

Appendix A: Description of FEER Emission

The NASA Fire Energetics and Emissions Research (FEER) emission data set is based on a top-down approach (Ichoku & Ellison, 2014) and is available for public at <http://feer.gsfc.nasa.gov/>. Equations (3) and (4) in the text show the fundamental formula used in FEER algorithm. The global gridded coefficients C_e (or product of $\alpha \cdot \beta_s$ in equation (3)) for smoke total particulate matter (TPM) is first derived based on the method originally proposed by Ichoku and Kaufman (2005). In the current FEER version 1.0 emission data set (FEER v1.0), FEER uses the coincident C_e and time-integrated FRP data from GFAS version 1.0 (Kaiser et al., 2012) to estimate the total amount of TPM emitted at each gridbox (thus the name: FEER v1.0-G1.0). The emission factors (EFs) of other fire emission species from Andreae and Merlet (2001, updated in 2014) are then used to derive their respective emission ratios relative to TPM at various land cover types in order to estimate the C_e for these other species (such as organic and black carbon). Both the FRP and AOD data used to generate the gridded FEER.v1 C_e (that links FRP to TPM) are derived from MODIS on Terra (MOD14 and MOD04_L2) and Aqua (MYD14 and MYD04_L2) satellites. In order to distinguish the background and smoke plume AOD, the Modern Era Retrospective-Analysis for Research and Applications wind vector at 850 mb data set is used in the algorithm (Ichoku & Ellison, 2014; Ichoku & Kaufman, 2005) to estimate the time to emit the mass of smoke aerosol by a certain plume. The linear relationship between FRP and the rate of smoke emission is then determined to obtain the gridded ($1^\circ \times 1^\circ$) C_e products (Andreae & Merlet, 2001; Ichoku & Ellison, 2014; Ichoku & Kaufman, 2005). FEERv1.0-G1.0 is the first biomass burning emission derived from global gridded emission coefficient products. Thus, prior knowledge of the ecosystem type of an active fire is not required from the user, as it is implicit in the grid location of the emission data. Furthermore, while the emission coefficients were derived using only daytime measurements because AOD is only measured during the daytime, FEER provides nighttime fire emissions, assuming that the coefficient for any location is applicable to both daytime and nighttime.

Acknowledgments

This research was funded by NASA under its Research Opportunities in Space and Earth Sciences (ROSES)—2009 and 2013 Interdisciplinary Studies (IDS) Program (Jack Kaye, Earth Science Research Director) through the Radiation Sciences Program managed by Hal Maring. J. Wang also received the support from the NASA Applied Science Program (air quality focus area) managed by John A. Haynes and the Suomi-NPP program. AERONET data are downloaded from <http://aeronet.gsfc.nasa.gov>. The MODIS aerosol and active fire products are available from the Level-1 and Atmosphere Archive and Distribution System (LAADS) website (<http://ladsweb.nascom.nasa.gov>) and the University of Maryland website (<ftp://fuoco.geog.umd.edu>), respectively. The CALIPSO data are from the Atmospheric Science Data Center (ASDC) website (<https://eosweb.larc.nasa.gov>). FEER emission data can be obtained from <https://feer.gsfc.nasa.gov/data/>. All the modeling data presented for the figures in this manuscript will be made available through Coalition on Publishing Data in the Earth and Space Sciences (<https://copdessdirectory.osf.io>) and please e-mail J. Wang (jun-wang-1@uiowa.edu) for details.

References

- Ackerman, S. A., Strabala, K. I., Menzel, W. P., Frey, R. A., Moeller, C. C., & Gumley, L. E. (1998). Discriminating clear sky from clouds with MODIS. *Journal of Geophysical Research*, 103, 32,141–32,157.
- Ackermann, I. J., Hass, H., Memmesheimer, M., Ebel, A., Binkowski, F. S., & Shankar, U. (1998). Modal aerosol dynamics model for Europe: Development and first applications. *Atmospheric Environment*, 32, 2981–2999.
- Anderson, J. C., Wang, J., Zeng, J., Leptoukh, G., Petrenko, M., Ichoku, C., & Hu, C. (2013). Long-term statistical assessment of Aqua-MODIS aerosol optical depth over coastal regions: Bias characteristics and uncertainty sources. *Tellus B*, 65, 20805. <https://doi.org/10.3402/tellusb.6510.20805>
- Andreae, M., Andreae, T. W., Annegarn, H., Beer, J., Cachier, H., Le Canut, P., ... Zenker, T. (1998). Airborne studies of aerosol emissions from savanna fires in southern Africa: 2. Aerosol chemical composition. *Journal of Geophysical Research*, 103, 32,119–32,128.
- Andreae, M. O. (1991). Biomass burning: Its history, use, and distribution and its impact on environmental quality and global climate. *Global Biomass Burning: Atmospheric, Climatic and Biospheric Implications*, 3–21.
- Andreae, M. O., Browell, E. V., Garstang, M., Gregory, G. L., Harriss, R. C., Hill, G. F., ... Wofsy, S. C. (1988). Biomass-burning emissions and associated haze layers over Amazonia. *Journal of Geophysical Research*, 93(D2), 1509–1527.
- Andreae, M. O., & Merlet, P. (2001). Emission of trace gases and aerosols from biomass burning. *Global Biogeochemical Cycles*, 15, 955–966.
- Bird, M., & Cali, J. (1998). A million-year record of fire in sub-Saharan Africa. *Nature*, 394, 767–769.
- Boubel, R. W., Darley, E. F., & Schuck, E. A. (1969). Emissions from burning grass stubble and straw. *Journal of the Air Pollution Control Association*, 19, 497–500.
- Bowman, D. M. J. S., Balch, J. K., Artaxo, P., Bond, W. J., Carlson, J. M., Cochrane, M. A., ... Pyne, S. J. (2009). Fire in the Earth system. *Science*, 324, 481–484.
- Brass, J. A., Guild, L. S., Riggan, P. J., Ambrosia, V. G., Lockwood, R. N., Joao, A. P. H., & Higgins, R. G. (1996). Characterizing Brazilian fire and estimating areas burned by using the Airborne Infrared Disaster Assessment System. In J. S. Levine (Ed.), *Biomass Burning and Global Change: Vol. 2 Biomass Burning in South America, Southeast Asia, and Temperate and Boreal Ecosystems, and the Oil Fires of Kuwait* (pp. 561–568). Cambridge, MA: MIT Press.
- Cardoso, M. F., Hurr, G. C., Moore, B., Nobre, C. A., & Prins, E. M. (2003). Projecting future fire activity in Amazonia. *Global Change Biology*, 9, 656–669.
- Chen, F., & Dudhia, J. (2001). Coupling an advanced land surface-hydrology model with the Penn State-NCAR MM5 modeling system. Part I: Model implementation and sensitivity. *Monthly Weather Review*, 129, 569–585.
- Chou, M.-D., Suarez, M. J., Ho, C.-H., Yan, M. M., & Lee, K.-T. (1998). Parameterizations for cloud overlapping and shortwave single-scattering properties for use in general circulation and cloud ensemble models. *Journal of Climate*, 11, 202–214.
- Christian, T. J., Kleiss, B., Yokelson, R. J., Holzinger, R., Crutzen, P. J., Hao, W. M., ... Ward, D. E. (2003). Comprehensive laboratory measurements of biomass-burning emissions: 1. Emissions from Indonesian, African, and other fuels. *Journal of Geophysical Research*, 108, 4719. <https://doi.org/10.1029/2003JD003704>
- Crutzen, P. J., & Andreae, M. O. (1990). Biomass burning in the tropics: Impact on atmospheric chemistry and biogeochemical cycles. *Science*, 250, 1669–1678.
- Crutzen, P. J., Heidt, L. E., Krasnec, J. P., Pollock, W. H., & Seiler, W. (1979). Biomass burning as a source of atmospheric gases CO, H₂, N₂O, NO, CH₃Cl and COS. *Nature*, 282, 253–256.
- Darley, E. F., Burleson, F., Mateer, E., Middleton, J. T., & Osterli, V. (1966). Contribution of burning of agricultural wastes to photochemical air pollution. *Journal of the Air Pollution Control Association*, 16, 685–690.
- Darmenov, A., & da Silva, A. (2013). The quick fire emissions dataset (QFED)—Documentation of versions 2.1, 2.2 and 2.4. *NASA Technical Report Series on Global Modeling and Data Assimilation*, NASA TM-2013-104606, 32, 183.
- Dubovik, O., Smirnov, A., Holben, B., King, M., Kaufman, Y., Eck, T., & Slutsker, I. (2000). Accuracy assessments of aerosol optical properties retrieved from Aerosol Robotic Network (AERONET) Sun and sky radiance measurements. *Journal of Geophysical Research*, 105, 9791–9806.
- Eck, T. F., Holben, B. N., Reid, J. S., Dubovik, O., Smirnov, A., O'Neill, N. T., ... Kinne, S. (1999). Wavelength dependence of the optical depth of biomass burning, urban, and desert dust aerosols. *Journal of Geophysical Research*, 104, 31,333–31,349.
- Fast, J. D., Gustafson, W. I., Easter, R. C., Zaveri, R. A., Barnard, J. C., Chapman, E. G., ... Peckham, S. E. (2006). Evolution of ozone, particulates, and aerosol direct radiative forcing in the vicinity of Houston using a fully coupled meteorology-chemistry-aerosol model. *Journal of Geophysical Research*, 111, D21305. <https://doi.org/10.1029/2005JD006721>
- Flannigan, M. D., & Haar, T. V. (1986). Forest fire monitoring using NOAA satellite AVHRR. *Canadian Journal of Forest Research*, 16, 975–982.
- Freeborn, P. H., Wooster, M. J., & Roberts, G. (2011). Addressing the spatiotemporal sampling design of MODIS to provide estimates of the fire radiative energy emitted from Africa. *Remote Sensing of Environment*, 115, 475–489.
- Gerstle, R., & Kemnitz, D. (1967). Atmospheric emissions from open burning. *Journal of the Air Pollution Control Association*, 17, 324–327.
- Giglio, L. (2010). *MODIS Collection 5 Active Fire Product User's Guide Version 2.4*. Science Systems and Applications, Inc.
- Giglio, L., Csiszar, I., & Justice, C. O. (2006). Global distribution and seasonality of active fires as observed with the Terra and Aqua Moderate Resolution Imaging Spectroradiometer (MODIS) sensors. *Journal of Geophysical Research*, 111, G02016. <https://doi.org/10.1029/2005JG000142>
- Giglio, L., Kendall, J., & Mack, R. (2003). A multi-year active fire dataset for the tropics derived from the TRMM VIRS. *International Journal of Remote Sensing*, 24, 4505–4525.
- Giglio, L., Randerson, J. T., & van der Werf, G. R. (2013). Analysis of daily, monthly, and annual burned area using the fourth-generation global fire emissions database (GFED4). *Journal of Geophysical Research: Biogeosciences*, 118, 317–328. <https://doi.org/10.1002/jgrg.20042>
- Grell, G., Freitas, S., Stuefer, M., & Fast, J. (2011). Inclusion of biomass burning in WRF-Chem: Impact of wildfires on weather forecasts. *Atmospheric Chemistry and Physics*, 11, 5289–5303.
- Grell, G. A., & Dévényi, D. (2002). A generalized approach to parameterizing convection combining ensemble and data assimilation techniques. *Geophysical Research Letters*, 29(14), 38–1–38–4. <https://doi.org/10.1029/2002GL015311>
- Grell, G. A., Peckham, S. E., Schmitz, R., McKeen, S. A., Frost, G., Skamarock, W. C., & Eder, B. (2005). Fully coupled “online” chemistry within the WRF model. *Atmospheric Environment*, 39, 6957–6975.
- Hao, W. M., & Liu, M.-H. (1994). Spatial and temporal distribution of tropical biomass burning. *Global Biogeochemical Cycles*, 8, 495–503.
- Heald, C. L., Jacob, D. J., Palmer, P. I., Evans, M. J., Sachse, G. W., Singh, H. B., & Blake, D. R. (2003). Biomass burning emission inventory with daily resolution: Application to aircraft observations of Asian outflow. *Journal of Geophysical Research*, 108(D21), 8811. <https://doi.org/10.1029/2002JD003082>

- Hoelzemann, J. J., Schultz, M. G., Brasseur, G. P., Granier, C., & Simon, M. (2004). Global Wildland Fire Emission Model (GWEM): Evaluating the use of global area burnt satellite data. *Journal of Geophysical Research*, 109, D14S04. <https://doi.org/10.1029/2003JD003666>
- Holben, B. N., Eck, T. F., Slutsker, I., Tanré, D., Buis, J. P., Setzer, A., ... Smirnov, A. (1998). AERONET—A federated instrument network and data archive for aerosol characterization. *Remote Sensing of Environment*, 66, 1–16.
- Hong, S.-Y., Noh, Y., & Dudhia, J. (2006). A new vertical diffusion package with an explicit treatment of entrainment processes. *Monthly Weather Review*, 134, 2318–2341.
- Hyer, E., Reid, J., & Zhang, J. (2011). An over-land aerosol optical depth data set for data assimilation by filtering, correction, and aggregation of MODIS Collection 5 optical depth retrievals. *Atmospheric Measurement Techniques*, 4, 379–408.
- Hyer, E., Wang, J., & Arellano, A. (2012). Biomass burning: Observations, modeling, and data assimilation. *Bulletin of the American Meteorological Society*, 93, ES10.
- Ichoku, C., Chu, D. A., Mattoo, S., Kaufman, Y. J., Remer, L. A., Tanré, D., ... Holben, B. N. (2002). A spatio-temporal approach for global validation and analysis of MODIS aerosol products. *Geophysical Research Letters*, 29(12), MOD1-1–MOD1-4. <https://doi.org/10.1029/2001GL013206>
- Ichoku, C., Ellison, L. T., Willmot, K. E., Matsui, T., Dezfali, A. K., Gatebe, C. K., ... Habib, S. (2016). Biomass burning, land-cover change, and the hydrological cycle in Northern sub-Saharan Africa. *Environmental Research Letters*, 11(9). <https://doi.org/10.1088/1748-9326/11/9/095005>
- Ichoku, C., & Ellison, L. (2014). Global top-down smoke-aerosol emissions estimation using satellite fire radiative power measurements. *Atmospheric Chemistry and Physics*, 14, 6643–6667.
- Ichoku, C., Giglio, L., Wooster, M. J., & Remer, L. A. (2008). Global characterization of biomass-burning patterns using satellite measurements of fire radiative energy. *Remote Sensing of Environment*, 112, 2950–2962.
- Ichoku, C., Kahn, R., & Chin, M. (2012). Satellite contributions to the quantitative characterization of biomass burning for climate modeling. *Atmospheric Research*, 111, 1–28.
- Ichoku, C., & Kaufman, Y. J. (2005). A method to derive smoke emission rates from MODIS fire radiative energy measurements. *Geoscience and Remote Sensing, IEEE Transactions on*, 43, 2636–2649.
- Ichoku, C., Martins, J. V., Kaufman, Y. J., Wooster, M. J., Freeborn, P. H., Hao, W. M., ... Nordgren, B. L. (2008). Laboratory investigation of fire radiative energy and smoke aerosol emissions. *Journal of Geophysical Research*, 113, D14S09. <https://doi.org/10.1029/2007JD009659>
- Ito, A., & Penner, J. E. (2004). Global estimates of biomass burning emissions based on satellite imagery for the year 2000. *Journal of Geophysical Research*, 109, D14S05. <https://doi.org/10.1029/2003JD004423>
- Justice, C. O., Giglio, L., Korontzi, S., Owens, J., Morisette, J. T., Roy, D., ... Kaufman, Y. (2002). The MODIS fire products. *Remote Sensing of Environment*, 83, 244–262.
- Kaiser, J. W., Flemming, J., Schultz, M. G., Suttie, M., & Wooster, M. J. (2009). The MACC Global Fire Assimilation System: First Emission Products (GFASv0). ECMWF Technical Memorandum (No. 596). Reading, UK: European Centre for Medium-Range Weather Forecasts.
- Kaiser, J. W., Heil, A., Andreae, M. O., Benedetti, A., Chubarova, N., Jones, L., ... van der Werf, G. R. (2012). Biomass burning emissions estimated with a global fire assimilation system based on observed fire radiative power. *Biogeosciences*, 9, 527–554.
- Kalnay, E., Kanamitsu, M., Kistler, R., Collins, W., Deaven, D., Gandin, L., ... Joseph, D. (1996). The NCEP/NCAR 40-year reanalysis project. *Bulletin of the American Meteorological Society*, 77, 437–471.
- Kauffman, J. B., Steele, M. D., Cummings, D. L., & Jaramillo, V. J. (2003). Biomass dynamics associated with deforestation, fire, and conversion to cattle pasture in a Mexican tropical dry forest. *Forest Ecology and Management*, 176, 1–12.
- Kaufman, Y. J., Justice, C. O., Flynn, L. P., Kendall, J. D., Prins, E. M., Giglio, L., ... Setzer, A. W. (1998). Potential global fire monitoring from EOS-MODIS. *Journal of Geophysical Research*, 103, 32,215–32,238.
- Levine, J. S. (1991). *Global Biomass Burning: Atmospheric, Climatic, and Biospheric Implications*. MIT press.
- Levy, R., Mattoo, S., Munchak, L., Remer, L., Sayer, A., & Hsu, N. (2013). The Collection 6 MODIS aerosol products over land and ocean. *Atmospheric Measurement Techniques*, 6, 2989–3034.
- Levy, R. C., Remer, L. A., Kleidman, R. G., Mattoo, S., Ichoku, C., Kahn, R., & Eck, T. (2010). Global evaluation of the Collection 5 MODIS dark-target aerosol products over land. *Atmospheric Chemistry and Physics*, 10, 10,399–10,420.
- Lighty, J. S., Veranth, J. M., & Sarofim, A. F. (2000). Combustion aerosols: Factors governing their size and composition and implications to human health. *Journal of the Air & Waste Management Association*, 50, 1565–1618.
- Lin, Y.-L., Farley, R. D., & Orville, H. D. (1983). Bulk parameterization of the snow field in a cloud model. *Journal of Climate and Applied Meteorology*, 22, 1065–1092.
- Liu, Z., Vaughan, M. A., Winker, D. M., Hostetler, C. A., Poole, L. R., Hlavka, D., ... McGill, M. (2004). Use of probability distribution functions for discriminating between cloud and aerosol in lidar backscatter data. *Journal of Geophysical Research*, 109, D15202. <https://doi.org/10.1029/2004JD004732>
- Liu, Z., Vaughan, M., Winker, D., Kittaka, C., Getzewich, B., Kuehn, R., ... Hostetler, C. (2009). The CALIPSO Lidar Cloud and Aerosol Discrimination: Version 2 Algorithm and Initial Assessment of Performance. *Journal of Atmospheric and Oceanic Technology*, 26, 1198–1213. <https://doi.org/10.1175/2009JTECHA1229.1>
- Malaver, E. J., Taubman, S. J., Brown, P. D., Iacono, M. J., & Clough, S. A. (1997). Radiative transfer for inhomogeneous atmospheres: RRTM, a validated correlated-k model for the longwave. *Journal of Geophysical Research*, 102, 16,663–16,682.
- Peterson, D., & Wang, J. (2013). A Sub-pixel-based calculate of fire radiative power from MODIS observations: 2. Sensitivity analysis and potential fire weather application. *Remote Sensing of Environment*, 129, 231–249.
- Peterson, D., Wang, J., Ichoku, C., Hyer, E., & Ambrosia, V. (2013). A sub-pixel-based calculate of fire radiative power from MODIS observations: 1. Algorithm development and validation. *Remote Sensing of Environment*, 129, 262–279.
- Platnick, S., Meyer, K. G., King, M. D., Wind, G., Amarasinghe, N., Marchant, B., ... Yang, P. (2017). The MODIS cloud optical and micro-physical products: Collection 6 updates and examples from Terra and Aqua. *IEEE Transactions on Geoscience and Remote Sensing*, 55(1), 502–525.
- Polivka, T., Wang, J., Ellison, L., Hyer, E., & Ichoku, C. (2016). Improving nocturnal fire detection with the VIIRS day-night band. *IEEE Transactions on Geoscience and Remote Sensing*, 9, 5503–5519.
- Power, M. J., Marlon, J., Ortiz, N., Bartlein, P. J., Harrison, S. P., Mayle, F. E., ... Zhang, J. H. (2008). Changes in fire regimes since the Last Glacial Maximum: An assessment based on a global synthesis and analysis of charcoal data. *Climate Dynamics*, 30, 887–907.
- Prins, E. M., & Menzel, W. (1992). Geostationary satellite detection of bio mass burning in South America. *International Journal of Remote Sensing*, 13, 2783–2799.
- Prins, E. M., & Menzel, W. P. (1994). Trends in South American biomass burning detected with the GOES visible infrared spin scan radiometer atmospheric sounder from 1983 to 1991. *Journal of Geophysical Research*, 99, 16,719–16,735.

- Reid, J., Koppmann, R., Eck, T., & Eleuterio, D. (2005). A review of biomass burning emissions part II: Intensive physical properties of biomass burning particles. *Atmospheric Chemistry and Physics*, 5, 799–825.
- Reid, J. S., Prins, E. M., Westphal, D. L., Schmidt, C. C., Richardson, K. A., Christopher, S. A., ... Hoffman, J. P. (2004). Real-time monitoring of South American smoke particle emissions and transport using a coupled remote sensing/box-model approach. *Geophysical Research Letters*, 31, L06107. <https://doi.org/10.1029/2003GL018845>
- Reid, J. S., Hyer, E. J., Prins, E. M., Westphal, D. L., Zhang, J., Wang, J., ... Hoffman, J. P. (2009). Global monitoring and forecasting of biomass-burning smoke: Description of and lessons from the Fire Locating and Modeling of Burning Emissions (FLAMBE) program. *Selected Topics in Applied Earth Observations and Remote Sensing, IEEE Journal of*, 2, 144–162.
- Remer, L. A., Kleidman, R. G., Levy, R. C., Kaufman, Y. J., Tanré, D., Mattoo, S., ... Holben, B. N. (2008). Global aerosol climatology from the MODIS satellite sensors. *Journal of Geophysical Research*, 113, D14S07. <https://doi.org/10.1029/2007JD009661>
- Roberts, G., Wooster, M., & Lagoudakis, E. (2009). Annual and diurnal african biomass burning temporal dynamics. *Biogeosciences*, 6.
- Roberts, G., Wooster, M. J., Perry, G. L., Drake, N., Rebelo, L. M., & Dipotso, F. (2005). Retrieval of biomass combustion rates and totals from fire radiative power observations: Application to southern Africa using geostationary SEVIRI imagery. *Journal of Geophysical Research*, 110, D21111. <https://doi.org/10.1029/2005JD006018>
- Roberts, G. J., & Wooster, M. J. (2008). Fire detection and fire characterization over Africa using Meteosat SEVIRI. *Geoscience and Remote Sensing, IEEE Transactions on*, 46, 1200–1218.
- Robinson, J. M. (1991). Fire from space: Global fire evaluation using infrared remote sensing. *International Journal of Remote Sensing*, 12, 3–24.
- Saide, P. E., Peterson, D. A., da Silva, A., Anderson, B., Ziemba, L. D., Diskin, G., ... Carmichael, G. R. (2015). Revealing important nocturnal and day-to-day variations in fire smoke emissions through a multiplatform inversion. *Geophysical Research Letters*, 42, 3609–3618. <https://doi.org/10.1002/2015GL063737>
- Sandberg, D., Pickford, S., & Darley, E. (1975). Emissions from slash burning and the influence of flame retardant chemicals. *Journal of the Air Pollution Control Association*, 25, 278–281.
- Sayer, A., Hsu, N., Bettenhausen, C., & Jeong, M. J. (2013). Validation and uncertainty estimates for MODIS Collection 6 “Deep Blue” aerosol data. *Journal of Geophysical Research: Atmospheres*, 118, 7864–7872. <https://doi.org/10.1002/jgrd.50600>
- Schell, B., Ackermann, I. J., Hass, H., Binkowski, F. S., & Ebel, A. (2001). Modeling the formation of secondary organic aerosol within a comprehensive air quality model system. *Journal of Geophysical Research*, 106, 28,275–28,293. <https://doi.org/10.1029/2001JD000384>
- Schmit, T. J., Griffith, P., Gunshor, M. M., Daniels, J. M., Goodman, S. J., & Lebar, W. J. (2016). A closer look at the ABI on the GOES-R series. *Bulletin of the American Meteorological Society*, 98(4), 681–698.
- Schroeder, W., Csiszar, I., & Morissette, J. (2008). Quantifying the impact of cloud obscuration on remote sensing of active fires in the Brazilian Amazon. *Remote Sensing of Environment*, 112, 456–470.
- Schüle, W. (1990). Landscapes and climate in prehistory: Interactions of wildlife, man, and fire. In *Fire in the Tropical Biota* (pp. 273–318). Springer.
- Scott, A. C., & Glasspool, I. J. (2006). The diversification of Paleozoic fire systems and fluctuations in atmospheric oxygen concentration. *Proceedings of the National Academy of Sciences of the United States of America*, 103, 10,861–10,865.
- Seiler, W., & Crutzen, P. J. (1980). Estimates of gross and net fluxes of carbon between the biosphere and the atmosphere from biomass burning. *Climatic Change*, 2, 207–247.
- Shi, Y., Matsunaga, T., & Yamaguchi, Y. (2015). High-resolution mapping of biomass burning emissions in three tropical regions. *Environmental Science & Technology*, 49, 10,806–10,814.
- Shi, Y., Zhang, J., Reid, J., Hyer, E., & Hsu, N. (2013). Critical evaluation of the MODIS Deep Blue aerosol optical depth product for data assimilation over North Africa. *Atmospheric Measurement Techniques*, 6, 949–969.
- Stockwell, W. R., Middleton, P., Chang, J. S., & Tang, X. (1990). The second generation regional acid deposition model chemical mechanism for regional air quality modeling. *Journal of Geophysical Research*, 95, 16,343–16,367.
- Tosca, M., Diner, D., Garay, M., & Kalashnikova, O. (2014). Observational evidence of fire-driven reduction of cloud fraction in tropical Africa. *Journal of Geophysical Research: Atmospheres*, 119, 8418–8432. <https://doi.org/10.1002/2014JD021759>
- van der Werf, G. R., Randerson, J. T., Giglio, L., Collatz, G. J., Mu, M., Kasibhatla, P. S., ... van Leeuwen, T. T. (2010). Global fire emissions and the contribution of deforestation, savanna, forest, agricultural, and peat fires (1997–2009). *Atmospheric Chemistry and Physics*, 10, 11,707–11,735.
- van der Werf, G. R., Randerson, J. T., Giglio, L., Collatz, G. J., Kasibhatla, P. S., & Arellano, A. F. Jr. (2006). Interannual variability in global biomass burning emissions from 1997 to 2004. *Atmospheric Chemistry and Physics*, 6, 3423–3441.
- van der Werf, G. R., Randerson, J. T., Giglio, L., van Leeuwen, T. T., Chen, Y., Rogers, B. M., ... Kasibhatla, P. S. (2017). Global fire emissions estimates during 1997–2016. *Earth System Science Data*, 9, 697–720. <https://doi.org/10.5194/essd-9-697-2017>
- Vermote, E., & Roy, D. (2002). Land surface hot-spot observed by MODIS over Central Africa. *International Journal of Remote Sensing*, 23, 2141–2143.
- Wang, J., Christopher, S. A., Nair, U., Reid, J. S., Prins, E. M., Szykman, J., & Hand, J. L. (2006). Mesoscale modeling of Central American smoke transport to the United States: 1. “Top-down” assessment of emission strength and diurnal variation impacts. *Journal of Geophysical Research*, 111, D05S17. <https://doi.org/10.1029/2005JD006416>
- Wang, J., Ge, C., Yang, Z., Hyer, E. J., Reid, J. S., Chew, B.-N., ... Zhang, M. (2013). Mesoscale modeling of smoke transport over the Southeast Asian Maritime Continent: Interplay of sea breeze, trade wind, typhoon, and topography. *Atmospheric Research*, 122(Supplement C), 486–503.
- Watson, C. E., Fishman, J., & Reichle, H. G. (1990). The significance of biomass burning as a source of carbon monoxide and ozone in the southern hemisphere tropics: A satellite analysis. *Journal of Geophysical Research*, 95, 16,443–16,450.
- Wiedinmyer, C., Akagi, S., Yokelson, R. J., Emmons, L., Al-Saadi, J., Orlando, J., & Soja, A. (2011). The Fire Inventory from NCAR (FINN): A high resolution global model to estimate the emissions from open burning. *Geoscientific Model Development*, 4, 625.
- Winker, D. M., Pelon, J., Coakley, J. A., Ackerman, S. A., Charlson, R. J., Colarco, P. R., ... Wielicki, B. A. (2010). The CALIPSO Mission: A Global 3D View of Aerosols and Clouds. *Bulletin of the American Meteorological Society*, 91(9), 1211–1229.
- Wooster, M. J. (2002). Small-scale experimental testing of fire radiative energy for quantifying mass combusted in natural vegetation fires. *Geophysical Research Letters*, 29(21), 2027. <https://doi.org/10.1029/2002GL015487>
- Yang, Z., Wang, J., Ichoku, C., Hyer, E., & Zeng, J. (2013). Mesoscale modeling and satellite observation of transport and mixing of smoke and dust particles over northern sub-Saharan African region. *Journal of Geophysical Research: Atmospheres*, 118, 12,139–12,157. <https://doi.org/10.1002/2013JD020644>

- Zhang, F., Jun, W., Charles, I., Edward, J. H., Zhifeng, Y., Cui, G., ... Arlindo da, S. (2014). Sensitivity of mesoscale modeling of smoke direct radiative effect to the emission inventory: A case study in northern sub-Saharan African region. *Environmental Research Letters*, 9, 075002.
- Zhang, J., & Reid, J. S. (2006). MODIS aerosol product analysis for data assimilation: Assessment of over-ocean level 2 aerosol optical thickness retrievals. *Journal of Geophysical Research*, 111, D22207. <https://doi.org/10.1029/2005JD006898>
- Zhang, X., Kondragunta, S., Ram, J., Schmidt, C., & Huang, H. C. (2012). Near-real-time global biomass burning emissions product from geostationary satellite constellation. *Journal of Geophysical Research*, 117, D14201. <https://doi.org/10.1029/2012JD017459>